Fall 12-18-2020

A Numerical and Experimental Study of Lid Driven Square Cavity Flow for Laminar and Turbulent Cases

Abdullah BIn Naeem
University of New Orleans, anaeem@uno.edu

A Numerical and Experimental Study of Lid Driven Square Cavity Flow for Laminar and Turbulent Cases

A Thesis

Submitted to the Graduate Faculty of the

University of New Orleans

in partial fulfillment of the
requirements for the degree of

Master of Science
in
Engineering

(Mechanical)

By

Abdullah Bin Naeem

BS. University of Engineering & Technology Lahore, 2013
MS. University of New Orleans, 2020

December, 2020

DEDICATION

To

My Parents

Who brought me into this world and taught me to kept going no matter what and never give up on your dreams and passion

and

My Sister

Who has been a constant support and a source of motivation throughout my graduate program.

ACKNOWLEDGMENT

First, I would like to express my sincere gratitude to my advisor, Dr. Kazim M
Akyuzlu for his continuous support throughout my master's degree. His passion and enthusiasm is what kept me going and motivated me to finish this thesis and my degree. He has been a constant help throughout in my thesis, laboratory work and classes. His professionalism is admirable. He didn't just guide me through the academic journey at the University of New Orleans, but he helped me grow and develop skills that are important in all aspects of life.

I would also like to extend my gratitude to Dr Brandon Travella for allowing me to work for one his navel engineering projects.

Besides my advisor, I would like to thank the rest of my thesis committee; Dr. Ting Wang and Dr. Martin J Guillot for their encouragement and insightful comments.

A special thanks to my colleague Shivank who helped me in the Lab work and during my simulations. Last but not the least, I would like to thank my family, my father Chaudhry Muhammad Naeem and my mother Rafia Naeem for making me capable of coming this far and completing this work and last but not the least my sister who has been constant motivation and push to achieve all my goals in life.

ABSTRACT

Experimental and numerical studies are performed on steady and unsteady lid-driven cavity flow case for laminar flow regime. In the experiments, a PIV and an LDA were employed to measure the global and local velocities, respectively inside a cavity of AR 1.0. The velocity vector plots and streamline plots which represent unsteady circulation patterns are obtained using the PIV. The steady local velocities measured with LDA are then used to calibrate the PIV measurements. Numerical study is performed using a commercial CFD solver. For turbulent flow simulation RANS equations with K-Epsilon closure model were used. From the PIV calibration study, it can be observed that the characteristic of the horizontal velocity profile measured using PIV and predicted by CFD solver agrees with each other however both overestimates the ones given by LDA. In unsteady simulations, the lid acceleration was found to influence the development and movement of circulation centers.

TABLE OF CONTENTS

NOMENCLATURE

Symbols

AR	Aspect Ratio (H/L)
x	Axial/Streamwise Coordinate
H	Height of the Cavity
L	Length of the Cavity
u_o	Lid Speed
Pr	Prandtl Number
P	Pressure
C_p	Pressure Coefficient
Re	Reynolds Number
t	Time
y	Transverse Coordinate
K	Turbulent Kinetic Energy
Pr_k	Turbulent Prandtl Number
u	*x* velocity
v	y velocity

Greek Symbols

μ	Absolute Viscosity
$C\mu$	Coefficient of Eddy Viscosity
ρ	Density
μ_{eff}	Effective Viscosity
ν	Kinematic Viscosity
δ	Kronecker Delta
τ	Shear Stress
ϵ	Turbulent Dissipation Function
μ_t	Turbulent Viscosity

LIST OF FIGURES

LIST OF TABLES

1. INTRODUCTION

The lid driven cavity flow is widely used as a benchmark case to study computationally, internal flows, steady and unsteady. The simple geometry and easily imposed boundary conditions makes it very attractive for computational fluid dynamics researchers to validate their numerical codes. Extensive published work in the literature that relates to this topic is available. Results of this benchmarks case study are available for a large range of Reynolds numbers that can be referred to for establishing validity or run comparisons for developed numerical codes. In addition to its use as a benchmark case for the calibration of CFD solver for fluid flow simulations, the driven cavity flow problem also found place in industrial applications. It has been used to model and study industrial applications such as; film melt spinning processes used in manufacture microcrystalline materials [1] and continuous drying [2]. Driven cavity flows also have applications in nature. Such is the case in the modeling of sediment bed impurities [3]. A detail literature survey is provided in Chapter 2. In this work an experimental and numerical study is conducted on this case in laminar and turbulent flow regimes. The experimental setup built for this study is stationed in the Cryogenics Lab at the University of New Orleans. It comprises of a plexiglass cavity 1in wide 1in high and 5in deep to ensure 2D flow patterns. The cavity is filled with water and ten microns hollow glass sphere particles were used as seeding. The details of the experimental setup are provided in Chapter 3.

The experimental setup uses two non-intrusive flow measuring techniques, PIV & LDA. PIV is used to measure the global velocities in a flowing system. while LDA is used to make steady state local velocity measurements. This thesis work provided the opportunity to run a calibration study whereby the global velocity measurements taken from by the PIV were calibrated with LDA's local velocities measurements at points in the upper half of the cavity domain. The experimental results together with the calibration study is provided in Chapter 3.

A 3D cavity was also modeled in three dimensions using a commercial CFD modeler. The numerical prediction of the steady flow was made using a second order accurate (temporal & spatial)

implicit finite volume technique for solving the Naiver Stokes equation. The Reynolds Average Navier Stokes Equation (RANS) along with two equation closure model (Kϵ) were employed for numerical simulations of turbulent flow cases in the cavity. The details of the mathematical formulation can be found in Chapter 4.

Chapter 5 is dedicated to establishing the validity of the numerical solver settings. The numerical predictions have been compared with benchmark experimental and numerical solutions. It also includes mesh independence and time independent study to verify the accuracy and the convergence of the numerical method adapted for this study. (Fluent).

Chapter 6 provides the numerical simulations carried for the lid driven cavity flow for laminar and turbulent flow case using the settings against which the validation and verification was conducted in Chapter 5. Good turbulence model settings are established by performing a calibration study at the transition Reynolds Numbers.

In Chapter 7 the unsteady lid driven cavity flow is numerically simulated to see the effects that different lid accelerations have on the flow development. Also, the movement of primary circulation is tracked as the flow develops from stagnation to steady state.

Concluding remarks and recommendations for future work and improvements can be found in Chapter 8 and 9 respectively.

2. LITERATURE REVIEW

There are numerous studies both experimental and numerical conducted on lid driven cavity flow. These studies are presented here according to the following categorization: the type of non-intrusive technique employed, aspect ratio, range of Reynolds number, mathematical formulation and numerical method. Some research on the nonintrusive flow measuring equipment, PIV and LDA, used in this thesis is also included. For a start the reader is recommended to go through an overview of the flow physics of the lid driven cavity flow by Shankar & Deshpande [1]. They summarized the published work on experimental and computational studies of the lid driven cavity flow in two dimensions and three dimensions and explained the physics comprehensively. In experimental studies Kosseff and Street [3] uses Laser Doppler Anemometry for velocity measurements inside a cavity of aspect ratio one and later they extended their work to include the end wall effects in cavity flows at spanwise aspect ratio 1,2 and 3 and Reynolds number between 1000 to 10,000. Migeon used particle streak technique to study the development of Taylor-Gortler like vortices inside a square lid driven cavity [2]. In his experiments, a vertical wall acts as the driven lid. PIV techniques were used by Liberzon to study the effects of dilute polymers, ethylene oxide, for turbulent flows inside a lid driven cavity [8]. The use of PIV and LDA techniques to investigate shear driven flows in a similar experimental setup is reported by O'Hern et al. [9]. In their experiments, water is pumped across the top of a square cavity filled with water in order to induce motion in the cavity by shear forces. Flows where Reynolds numbers ranged from 100 to 900 were investigated in these experiments. Velocities calculated from the PIV and LDA readings were in good agreement inside the cavity but not so good near the walls. In the more recent works Faure [10] studies experimentally an open cavity flow driven by shear layer development between a boundary layer external flow and a recirculation is investigated with PIV for Reynolds number in the range 1900-12000 and aspect ratio between 0.5 to 2. His main findings were that the shear driven cavity flow is controlling the recirculating cavity flow by momentum injection and ejection causing the centrifugal instability development at a lower level.

Ghia et al. in 1982 [9] used a coupled strongly implicit multigrid method with a uniform mesh to solve the vorticity and stream function formulation of the Navier- Stokes equations for driven cavity flows at Reynolds numbers ranging from 1,000-10,000 for a fluid with Prandtl No 1. His work is considered as the benchmark study when it comes to numerical simulation of driven cavity flows.

Erturk and Gokcol carried out their steady, 2-D simulations of incompressible driven cavity flows at high Reynolds numbers, up to 21,000, using a fine computational mesh and a finite volume solver [10]. Barragy and Carey used a p-type finite element scheme to compute the stream-vorticity function for steady, incompressible flows inside a cavity for Reynolds numbers up to 12,500 [11]. Sahin and Owens used an implicit finite volume method to solve the governing equations of incompressible, lid driven cavity flows, for both steady and unsteady cases, and for Reynolds numbers up to 10,000 [12].

Benjamin & Denny [29] uses the lid driven cavity problem to examines the convergence properties for various finite difference schemes at very high Reynolds numbers. M. Nallasamy & K Krishna [32] solves the full Navier Stokes Equation and observes that flow at very high Reynolds Number (Re>30,000) clearly exhibits boundary layer character and the downstream secondary eddy grows and decays in a manner like the upstream one. The famous work from R Schreiber & H.B Keller [33] presents efficient numerical techniques of higher order accuracy to solve the driven cavity problem. More recently Charles-Henri Bruneau & Mazen Saad [34] provides accurate benchmark results for a wide Range of Reynolds Number both in steady state as well as for periodic solutions A review of various turbulence models used in Reynolds Average Navier Stokes Equation and their application to the prediction of internal flows is present in Nallasamy [17] Nagapetyan et al. [16] uses the Reynolds Average Navier Stokes Equation with different turbulence (Closure) models to solve turbulent flow in 2D and 3D lid driven cavity flow. They also tested their newly developed closure model against the industry standard Spalart Allmaras; Shear Stress Transport and k-w. Debabrat Samantaray and Manab Kumar Das [36] studies turbulent flows inside the lid driven cavity of multiple aspect ratios.

Direct Numerical simulation of the turbulent flow cases was performed by Leriche & Gavrilakis [13] for Re=10 000. Similarly, Pradhan & Kumaran used an even more computationally intensive direct

simulation Monte Carlo method (DSMC) to study 2D and 3D lid driven cavity with two opposite walls moving in opposite direction at different velocities for compressible turbulent and transition flows. [14]. In another attempt Deshpande and Milton simulated the 3D lid driven cavity directly using the Navier Stokes Equation and compares the results obtained at Re=3200 and Re 10,000 with experimental data [15]. Jordan & Ragab [30] uses Direct Numerical Simulations to predict 3D cavity flows at a moderate Reynolds number where the flow is laminar and Large Eddy Simulations for higher Reynolds Number. In another study [31] they again use the Large Eddy Simulations using dynamic modeling and found that the highest turbulent production level not only occurred within the downstream eddy region of the cavity, but also along the upper half of the downstream Penga et al [35] performs the direct numerical simulation about the transition process from laminar to chaotic flow in a square lid driven cavity and finds the onset of chaotic flow for Reynolds number greater than 11,000.

Wen-Tao et.al [27] made a comparison between computational study with an experimental study conducted by 2D PIV. The 2D velocity vector fields and contour plots obtained for swirling flows in cylindrical cavity with rotating bottom wall are obtained computationally using Large Eddy Simulations and RANS equitation with Standard k-ϵ and Realizable k-ϵ closure models along the vertical and horizontal plane for two Reynolds number i.e., 2616 and 6541. These computational results are then compared with the experimental results of PIV for the same parameters. Immer et al. [39] performs wind tunnel experimental measurement on a 2D open cavity under perpendicular incident flow using a time resolved sterio PIV. Guermond et al [40] compares experimental data and numerical results of impulsively started flows in a 3D rectangular lid driven cavity at Reynolds Number of 1000. Ozalpb et al [42] investigates flow structures in cavities of different shapes using the PIV. Adrian [23] goes over the development of the PIV technology over the past 20 years, discusses the current practices and explains where the technology is heading towards. Hadad. et al. [24] studies the effect of seeding size, surface coating and concentration on the turbulent flow properties using PIV/PTV and finds the influence that these parameters have on high Reynolds Number with the size of the particle having the greatest effect on the velocity and acceleration values. In a similar study Tsrong et al [25] studies the macroscopic rigid

particles suspended in a three-dimensional viscous flow using an experimental arrangement that involves PIV and compares it with the computational results. They examine the response of these particles by varying several experimental parameters. In another study a micro PIV is used to investigate the fluid flow out of a micro cavity.

3. EXPERIMENTAL STUDY

This chapter gives details about the experimental setup that includes the employment of PIV and LDA for velocity measurements inside the cavity flow domain. The experimental arrangement and the equipment settings that were used to run the experiment are also included. The reader can also find results from an experimental run at low Reynolds Number, laminar flow. In the last section the findings of the calibration study where the PIV measured global velocities were calibrated using local LDA measured ones can be found.

3.1 Introduction

The experimental setup which was employed to conduct the experiments is composed of the test article (square cavity), an impermeable rigid lid, the rail system for the lid, and the 2D PIV system and the 2D LDA system. The test article is made of quarter inch thick Plexiglas. The test section, the square cavity, has one inch (25.4 mm) high walls on each side with a span (length) of one inch (25.4 mm) which gives us an aspect ratio of 1. The width of the cavity is constructed to be 5 inches (127 mm) which results in a width-based aspect ratio of 5. This is enough to ensure a two-dimensional flow inside the cavity; that is, one can assume the effect of the walls (those normal to the motion of the lid) on the flow field inside the cavity is negligible. A pictorial view of the setup is shown in Figure 5. Configuration of the PIV system camera and laser sheet relative to the test article is presented in Figure 2. In this arrangement, the test section is elevated above the table top it stands to accommodate the illumination of the cavity from underneath. A rigid lid is made of quarter inch (6.4 mm) Plexiglas is 36 inches (914.4mm) long and 5-inch (127 mm) wide sits on a rail system attached to the rear (upstream) and front (downstream) sections of the cavity as shown in Figure 3. The working fluid is chosen to be deionized water at room temperature. It is seeded with silver-coated hollow glass spheres of average diameter of 10μm and a density of 1300 kg/m3.

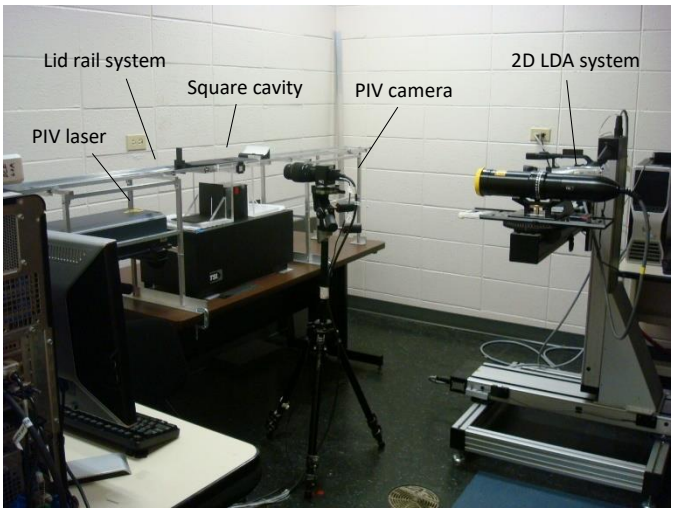

Figure 1 – Pictorial View of the Experimental Setup

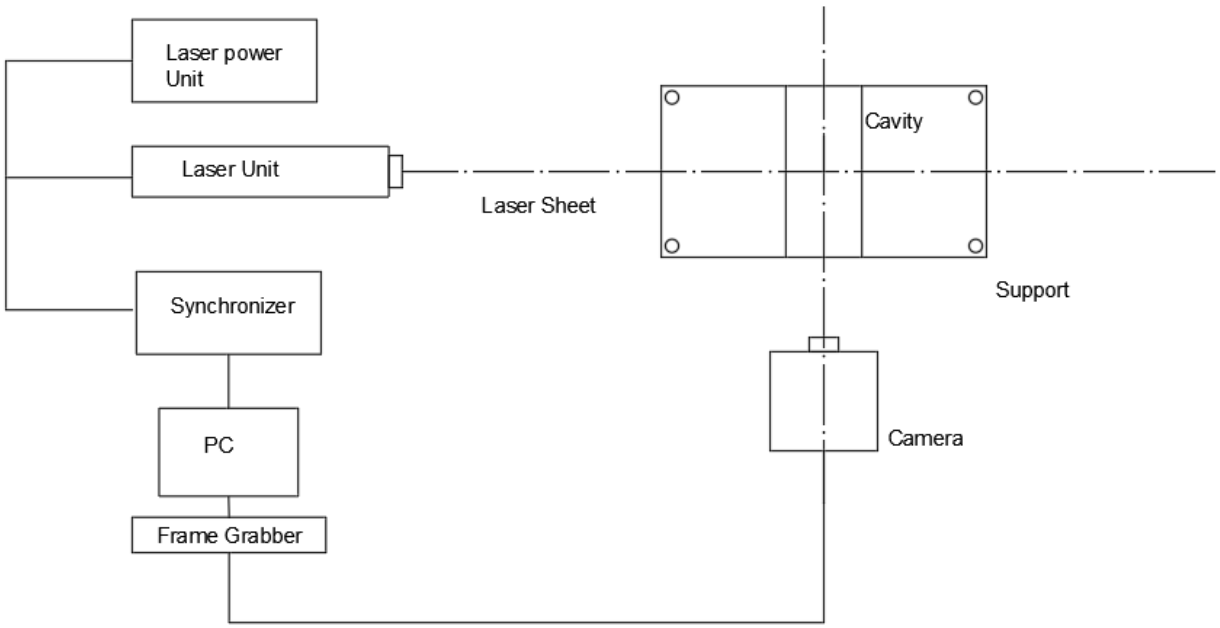

Figure 2 – Schematic of the PIV System

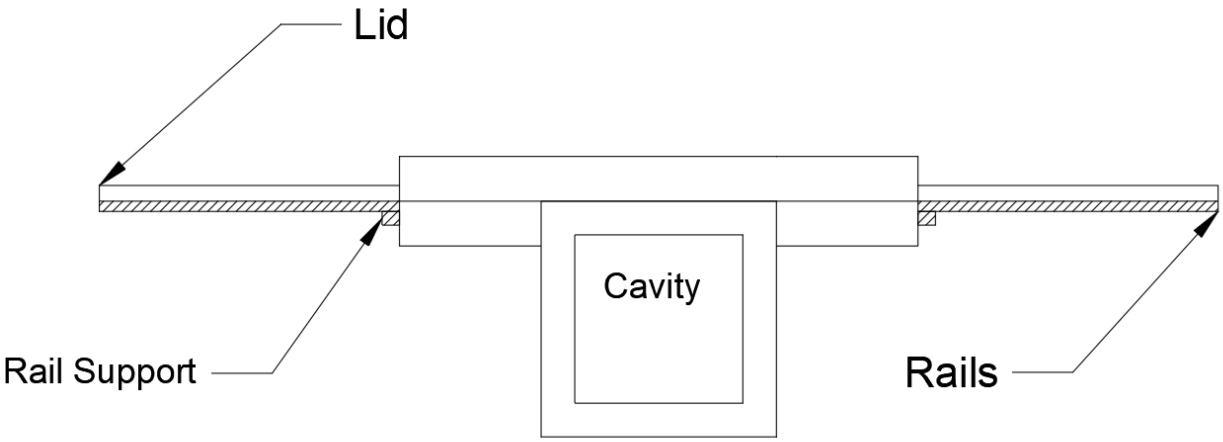

Figure 3 – Front View of the Cavity with Lid and Rails

3.2 PIV Settings

The nonintrusive velocity measurement system employed in the experimental study is a Two-Dimensional (2D) PIV system manufactured by TSI. The test section cavity is illuminated by a dual cavity 532 nm wavelength Nd-Yag laser unit with 500 mm lens. The laser is positioned normal to the test cavity's front face. The beam is bended at 45 degrees by a mirror replaced under the test cavity. The reflected beam then passes through a masking filter and finally illuminates the test section roughly at the center of the cavity width as shown in Figure 4. The camera is positioned normal to the test section square face and is placed at a distance where the illuminated cavity section is the focal point. The flow field images are captured by 2048 x 2048 pixels, high sensitivity CCD camera with a 105mm lens. Image processing unit (hardware and software) is by TSI. The reader interested in the specs of this unit should refer to reference [23]. An experimental procedure was established to ensure the repeatability of the experiments and accuracy of the experimental results. The reader is referred to reference [23] for the steps followed in conducting the experiments.

The choice of correct PIV settings is essential to making accurate velocity measurements. Therefore, various experiments were conducted to determine the proper PIV settings that were used in the planned experiments for the parametric study. The image capture settings are set to "straddle image" (giving dual framed images), a delta t (the time separating the two laser pulses) set to 1800μs, with a camera exposure time set of 2000 μs. The frame rate of the camera is set to 2.90 Hz. The image capture mode is set to "synchronized" (means that the image capturing, and laser pulsing will be governed and synchronized by the TSI synchronizer.) The number of images captured in the sequence is varied according to lid speed so that extraneous images are not captured after the lid has stopped moving. After the experiment, the images are masked to include the cavity only. The images are then processed with the software using a Hart's correlation, a Nyquist Grid, and a Gaussian Peak engine [16]. The images are processed with an interrogation area of 64 x 64 pixels and an overlay of 15%. No additional post-processing procedures were applied to the images.

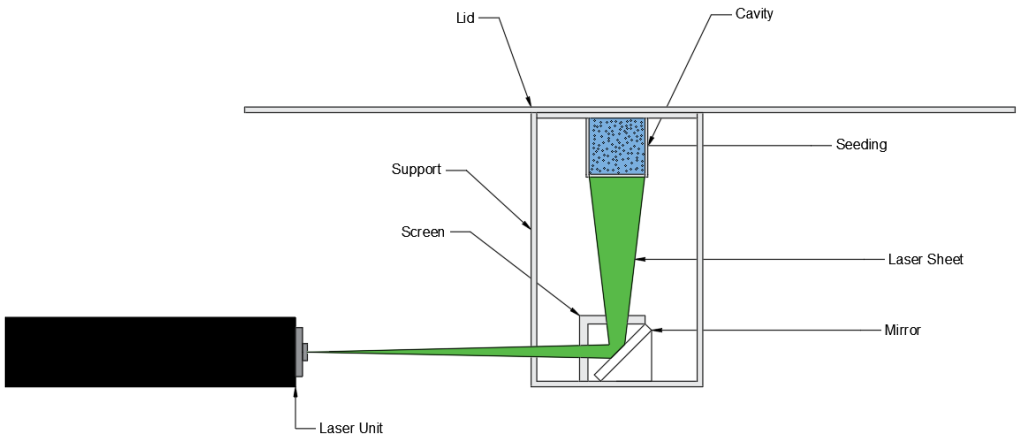

Figure 4 – Laser Sheet Projected Inside the Cavity with Water and Seeding

Table 1 – PIV Settings for the Experiment

Seeding (Water)	Silver coated hollow glass sphere particles with mean diameter of 10μm and a density of 1300kg/m^3
CCD Camera	High Sensitivity, 2048 x 2048 pixels (TSI PowerView), 105mm lens.
PIV Laser	Dual Cavity, 532nm wavelength Nd:Yag (Solo XT by New Wave) with 550 mm lens
Time Interval between Pulses	1800 μs
Interrogation Algorithm	Harts' Correlation
Interrogation Resolutions	64 x 64 Pixels
Interrogation Overlay	15% Vertical and Horizontal

3.3 LDA Settings

The other non-intrusive velocity measurement system employed to measure velocity locally is 2D LDA system manufactured by TSI. An Argon Ion Laser is used to generate single laser beam at about 600 mW, which is split into 4 beams using fiber light unit, manufactured by TSI. These 4 beams are then focused on fiber optics using optical couplers. The fiber optics connect couplers to the probe which targets the beam inside the cavity through 120 mm lens. The phenomenon of Doppler Effect measures the frequency of seeding particle, which is processed by LDA system processor and then converted to velocity at the local point under consideration. Statistical distribution of the velocity measurement is acquired through the LDA software, Flow Sizer. For the purpose of this study, number counts at local point for LDA velocity measurement is taken as 500 and the seeding used is silver-coated hollow glass sphere particles with mean diameter of 10μm. The schematic of the LDA setup is given in Figure 5. Choosing the correct settings are critical to the accuracy and reliability of the measured velocities. The fiber optic is set to back scatter mode. The downmix frequency is adjusted to 35 Hz. The PMT voltage is set to 450V and the burst threshold to 30mV. The SNR is kept very low and the band pass filter range is between 1-10MHz.

Table 2 – LDA Settings

LDA Settings	
Parameter	**Settings**
Fiber Optic Mode	Back Scatter
Downmix Frequency	35Hz
PMT Voltage	450V
Burst Threshold	30mV
Band Pass Filter	1-10Mhz

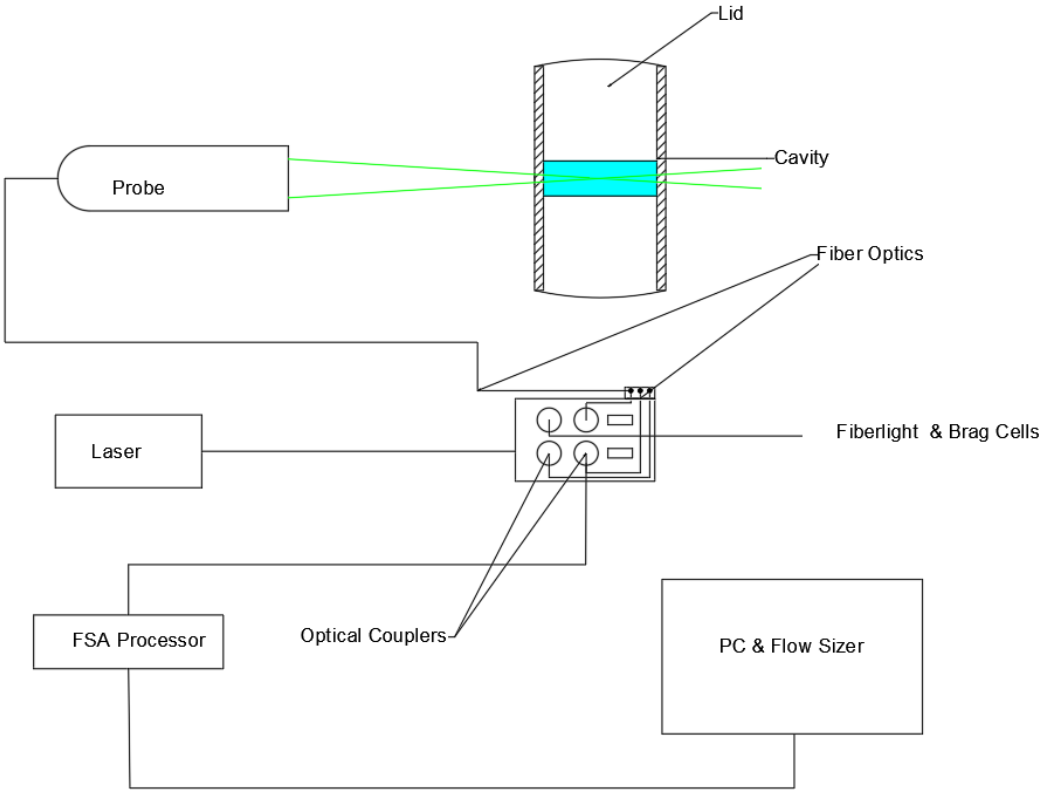

Figure 5 – Schematic of the LDA System

3.4 Experimental Results

Figure 6,7 and 8 shows the various processing stages on the PIV post processing software [21]. Starting with Figure 6, this figure shows the raw image of the flow domain captured by the CCD camera. The illuminated seedings can be clearly seen as shiny stars. As operations mode of the PIV software is set to straddle capture therefore two images A and B are captured separated by a time delay of DeltaT. (The value of DeltaT used in this experiment can be found in Table 1). Figure 7 is the image of the raw vector plot obtained after the PIV software processes images in frame A and frame B. Figure 8 is a refined version of the raw vector image that is generated by the plotting software that comes along with the PIV software.

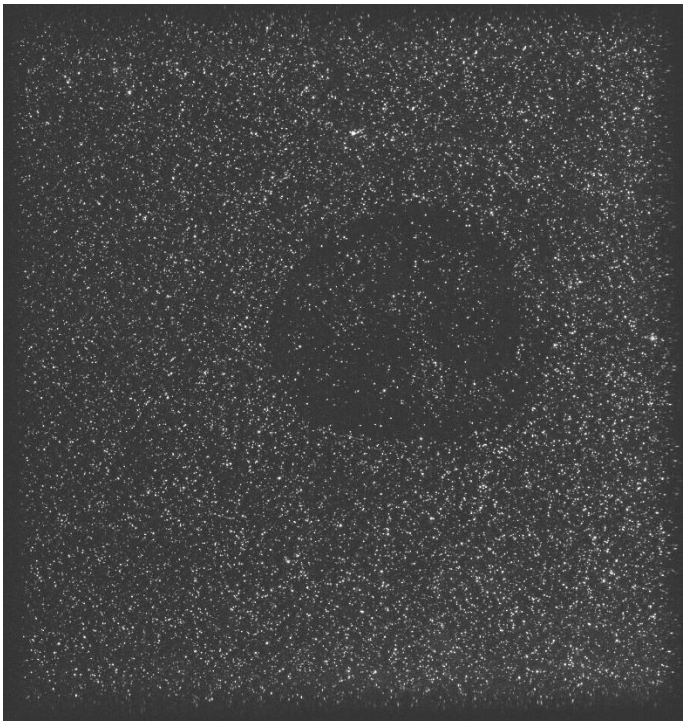

Figure 6 – Seeding Captured by the CCD Camera on Frame A

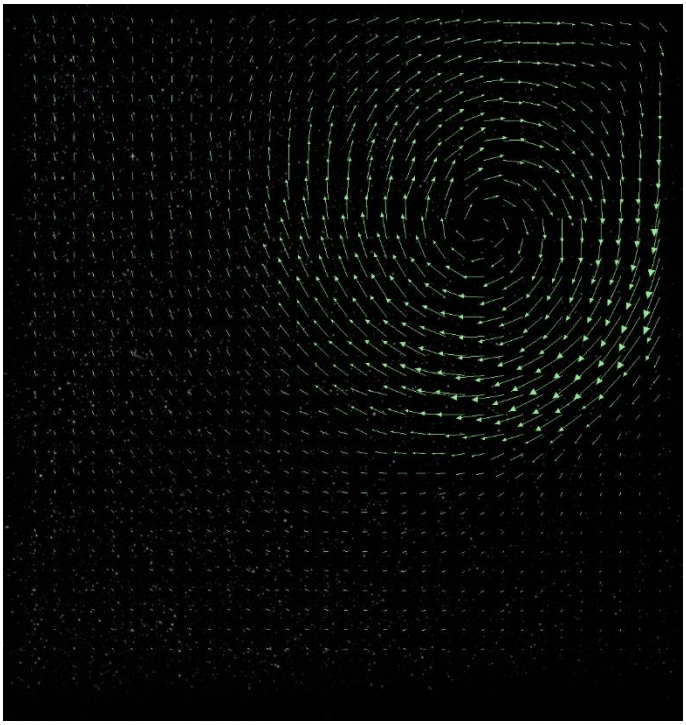

Figure 7 – Raw Vector Image Generated by PIV Post Processing Software

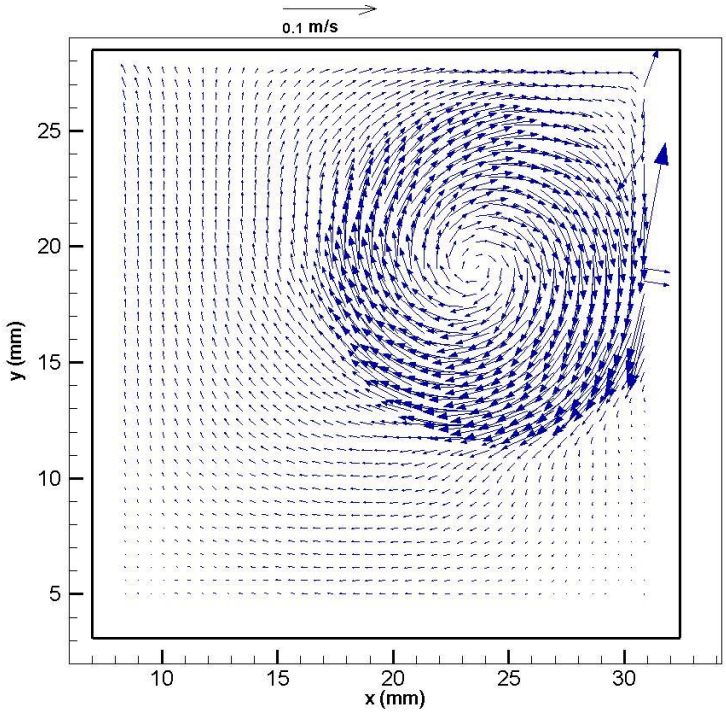

Figure 8 – Processed Vector Plot Generated by the Plotting Software.

3.5 Calibration of PIV Measured Velocities with LDA

The LDA captures the doppler shift in the frequencies as the seeding particles cuts the pointed laser beam at the point of measurement. The LDA thus provides precise values of velocities at a point in the flow domain. In contrast the PIV uses pulsed laser sheet to illuminate the flow domain while a synchronizer triggers the CCD camera to take two consecutive images of the flow domain. These images are fed to the processing software which runs statistical based algorithms to generate a velocity vector for each area of interrogation that the flow domain is divided into. All these vectors for all interrogation areas gives the velocity vector plots. The method described below is developed to calibrate the global velocity measurements obtained through the PIV with the local point velocities obtained by the LDA.

The calibration is performed on the vertical centerline of the upper half of the cavity domain. The results for the PIV experiments are taken from the works of John Farkas [21]. The data set taken from PIV and LDA in the calibration study are from velocity measurements at steady state. i.e. when the flow was fully developed. The results of the calibration study have been shown below. A third source of solution data that is referred to as CFD is discussed in extensive details in the later chapters of the thesis.

Velocity distribution across the cavity as observed by PIV and ones predicted by CFD are compared for Re=1250 at steady state in Figure 9. Similar comparison is made for Re=2030 and Re=3050 in Figure 10 and Figure 11. The velocity profiles, in the upper half of the vertical centerline of the cavity, observed experimentally (by LDA and PIV) and predicted numerically by the CFD solver are compared and presented in Figure 9 ,10 and 11. It can be observed that the characteristic of the horizontal velocity profile measured using PIV and predicted by CFD solver agrees however the ones measured by LDA are significantly underestimated.. It can be observed from Figure 9 and Figure 10, that as the Reynolds number is increased the deviation between horizontal velocities obtained by PIV and the ones predicted by CFD solver are reduced. However, a similar trend can be observed of CFD solver underpredicting the velocities measured by the PIV near to the center of the cavity at steady state. The LDA measurements for high Reynolds number fairs well with the PIV results near to the moving wall. It can be observed from

Figure 9 and 10 that as the Reynolds number is increased the percentage deviation between the maximum horizonal velocities measured by PIV and LDA is reduced.

Table 3 – Comparison of calculated (CFD) and measured (PIV and LDA) U velocities at vertical Centerline for Re=1250.

Y [mm]	**U By**		
	PIV [m/s]	LDA [m/s]	CFD [m/s]
0	-	-	0.04230
1	0.02660	0.01050	0.02213
2	0.02859	0.00900	0.01975
4	0.02777	0.00812	0.01544
6	0.02111	-	0.01082
8	0.00436	-	0.00641
10	-0.01024	-	0.00208
12	-0.01980	-	-0.00155
14	-0.02670	-	-0.00572

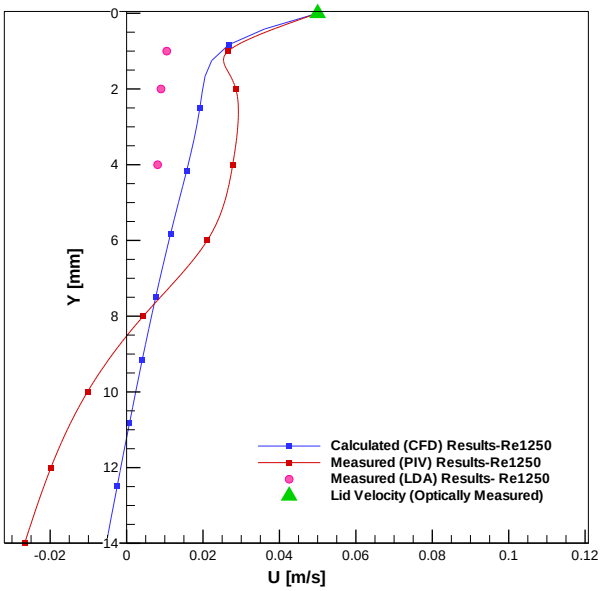

Figure 9 – Comparison of Calculated (CFD) and Measured (PIV and LDA) U Velocities on the Vertical Centerline at Re=1250

Table 4 – Comparison of calculated (CFD) and measured (PIV and LDA) U velocities at vertical Centerline for Re=2030.

Y [mm]	**U By**		
	PIV [m/s]	LDA [m/s]	CFD [m/s]
0		-	0.0885
1	0.0204	0.0250	0.0515
2	0.0225	0.0180	0.0483
4	0.0298	0.0170	0.0357
6	0.0244	-	0.0266
8	0.0089	-	0.0158
10	-0.0125	-	0.0061
12	-0.0219	-	-0.0031
14	-0.0318	-	-0.0120

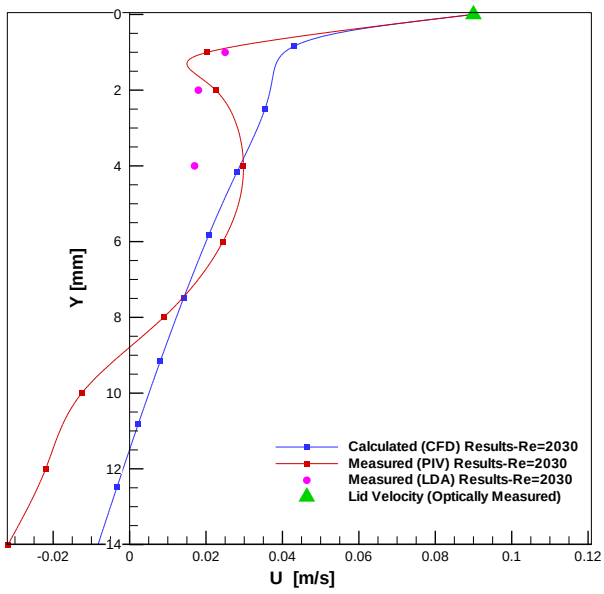

Figure 10 – Comparison of Calculated (CFD) and Measured (PIV and LDA) U velocities on the Vertical Centerline at Re=2030

Table 5 – Comparison of calculated (CFD) and measured (PIV and LDA) U velocities at vertical Centerline for Re=3050.

Y [mm]	**U By**		
	PIV [m/s]	LDA [m/s]	CFD [m/s]
0	-	-	0.1200
1	0.0145	0.02848	0.0427
2	0.0127	0.01149	0.0299
4	0.0117	0.00832	0.0249
6	0.0151	-	0.0188
8	0.0057	-	0.0118
10	-0.0028	-	0.0052
12	-0.0129	-	-0.0008
14	-0.0267	-	-0.0066

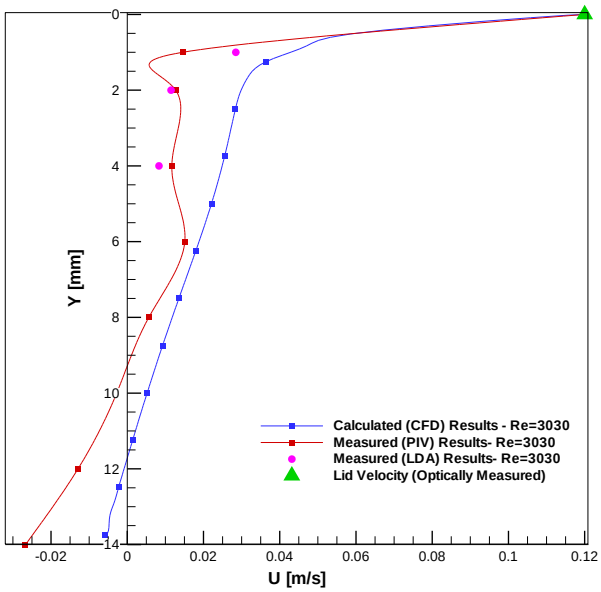

Figure 11 – Comparison of Calculated (CFD) and Measured (PIV and LDA) U Velocities on the Vertical Centerline at Re=3030

4. **MATHEMATICAL MODEL**

This chapter presents the mathematical model used by the commercial solver for numerical computations. The physical model is described first and is followed by the mathematical model. It includes the governing differential equations along with boundary conditions and initial conditions. For turbulent flow cases a separate set of equations (RANS) together with the K Epsilon closure model are presented.

4.1 Description of the Physical Model.

The experimental model is a 3D cavity made up of plexiglass. The details of the experimental model are given in Chapter 3. In this section the 2D physical model is described with all the assumptions to generate the mathematical formulation for the lid driven cavity flow. The model is a square cavity with Aspect Ratio = 1.0. The side walls and the bottom walls are stationary while the top wall or the lid is moving. The working fluid is water. The movement of the lid does not take out any water along with it and the volume of the working fluid always stays the same. The Reynolds number of the cavity is defined by the lid speed, so it is referred to as lid Reynolds number. The schematic below shows the physical model. The origin is taken to be as the bottom left corner of the cavity.

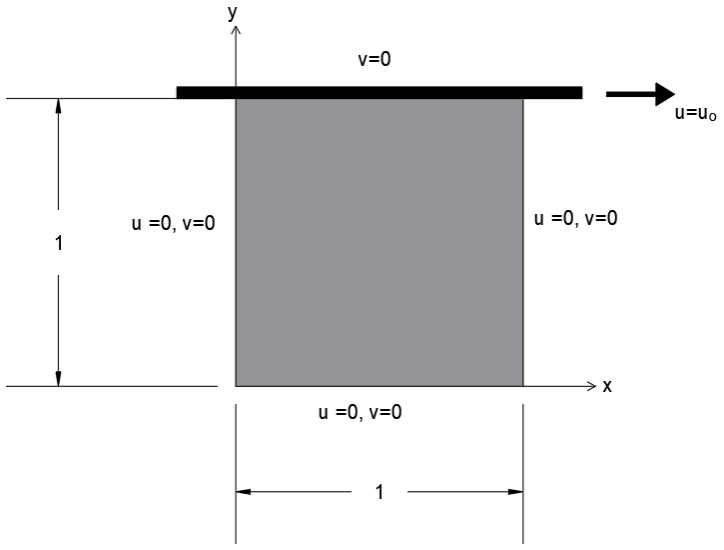

Figure 12 – Physical Model

4.2 Mathematical Model

The mathematical model comprises of the conservative form of the continuity and momentum equation together with the boundary conditions and the initial conditions making the problem a well posed one. The governing equations used to build the mathematical model are dimensional.

The following assumptions were made for the mathematical model:

1. The physical domain is two dimensional and the equations are in cartesian coordinates.
2. The working fluid forms a continuum.
3. The flow is subsonic, unsteady and viscous.
4. The working fluid is water which is incompressible with (Pr =7).
5. The working fluid behaves as a Newtonian fluid with stokes assumption.
6. The physical and transport properties are assumed to be constant.
7. No effect of gravity is assumed on the enclosed fluid.

4.2.1 Governing Differential Equation

For the physical model described in section 4.1 and the assumption taken in this section the following governing partial differential equations can be used to predict the flow fields. The equations in 2D cartesian coordinates for the physical model given in Figure 12 are shown below:

The continuity equation is given by:

$$\frac{\partial u}{\partial x} + \frac{\partial v}{\partial y} = 0 \tag{1}$$

The momentum equation in x direction is given by:

$$\frac{\partial}{\partial t}(u) + u\frac{\partial}{\partial x}(u) + v\frac{\partial}{\partial y}(u) = -\frac{1}{\rho}\frac{\partial p}{\partial x} + \nu\left(\frac{\partial^2 u}{\partial x^2} + \frac{\partial^2 u}{\partial y^2}\right) \tag{2}$$

The momentum equation in y direction is given by:

$$\frac{\partial}{\partial t}(v) + u\frac{\partial}{\partial x}(v) + v\frac{\partial}{\partial y}(v) = -\frac{1}{\rho}\frac{\partial p}{\partial y} + \nu\left(\frac{\partial^2 v}{\partial x^2} + \frac{\partial^2 v}{\partial y^2}\right) \quad (3)$$

4.2.2 Initial Conditions.

$$u = 0, v = 0 \; at \; t = 0 \; for \; 0 \le x \le L, 0 \le y \le H \quad (4)$$

4.2.3 Boundary Conditions.

$$u = 0, v = 0, \qquad at \; y = 0 \; and \; 0 \le x \le L \;\; for \;\; t > 0 \quad (5)$$

$$u = u_o, v = 0, \qquad at \; y = H \; and \; 0 \le x \le L \;\; for \;\; t > 0 \quad (6)$$

$$u = 0, v = 0, \qquad at \; x = 0 \; and \; 0 \le y \le H \;\; for \;\; t > 0 \quad (7)$$

$$u = 0, v = 0, \qquad at \; x = L \; and \; 0 \le y \le H \;\; for \;\; t > 0 \quad (8)$$

4.2.4 The Reynolds Average Navier Stokes Equation with K-Epsilon Turbulence Model

The momentum equation in the x-direction (flow direction):

$$\frac{\partial u}{\partial t} + \frac{\partial}{\partial x}(u) + \frac{\partial}{\partial y}(v) + \frac{1}{\rho}\frac{\partial p}{\partial x} = -\frac{1}{\rho}\left(\frac{\partial}{\partial x}\left[\mu_{eff}\frac{\partial u}{\partial x}\right] + \frac{\partial}{\partial y}\left[\mu_{eff}\frac{\partial u}{\partial y}\right]\right) = 0 \quad (9)$$

The momentum equation in the y-direction (traverse direction):

$$\frac{\partial v}{\partial t} + \frac{\partial}{\partial x}(uv) + \frac{\partial}{\partial y}(vv) + \frac{1}{\rho}\frac{\partial p}{\partial y} = -\frac{1}{\rho}\left(\frac{\partial}{\partial x}\left[\mu_{eff}\frac{\partial v}{\partial x}\right] + \frac{\partial}{\partial y}\left[\mu_{eff}\frac{\partial v}{\partial y}\right]\right) = 0 \quad (10)$$

Turbulence Model*:* The effective viscosity in the above equations is defined as:

$$\mu_{eff} = \mu + \mu_t \tag{11}$$

where the eddy viscosity is given by

$$\mu_t = \rho C_\mu \frac{K^2}{\varepsilon} \tag{12}$$

The turbulent kinetic energy is determined from:

$$\frac{\partial(K)}{\partial t} + \frac{\partial(uK)}{\partial x} + \frac{\partial(vK)}{\partial y} = \frac{1}{\rho}\frac{\partial}{\partial x}\left[\left(\mu + \frac{\mu_t}{\mathrm{Pr_k}}\right)\frac{\partial K}{\partial x}\right] + \frac{1}{\rho}\frac{\partial}{\partial y}\left[\left(\mu + \frac{\mu_t}{Pr_t}\right)\frac{\partial K}{\partial y}\right] + \frac{\mu_t}{\rho}\left[\left(\frac{\partial u}{\partial y} + \frac{\partial v}{\partial x}\right)^2 + 2\left(\frac{\partial u}{\partial x}\right)^2 + 2\left(\frac{\partial v}{\partial y}\right)^2\right]\varepsilon \tag{13}$$

The turbulent dissipation energy is determined from:

$$\frac{\partial(\varepsilon)}{\partial t} + \frac{\partial(u\varepsilon)}{\partial x} + \frac{\partial(v\varepsilon)}{\partial y} = \frac{1}{\rho}\frac{\partial}{\partial x}\left[\left(\mu + \frac{\mu_t}{\mathrm{Pr}_\epsilon}\right)\frac{\partial \varepsilon}{\partial x}\right] + \frac{1}{\rho}\frac{\partial}{\partial y}\left[\left(\mu + \frac{\mu_t}{\mathrm{Pr}_\epsilon}\right)\frac{\partial \varepsilon}{\partial y}\right] + C_{\varepsilon 1}\frac{\mu}{\rho}\frac{\varepsilon}{K}\left[\left(\frac{\partial u}{\partial y} + \frac{\partial v}{\partial x}\right)^2 + 2\left(\frac{\partial u}{\partial x}\right)^2 + 2\left(\frac{\partial v}{\partial y}\right)^2\right] - C_{\varepsilon 2}\frac{\varepsilon^2}{K} \tag{14}$$

The constants of the K- ε model adopted for this study are: $C_\mu = 0.09$, $Pr_K = 1.0$, $Pr_\varepsilon = 1.3$, $C_{\varepsilon 1} =$ 1.55, and $C_{\varepsilon 2} = 2.0$

5. VALIDATION AND VERIFICATION OF THE NUMERICAL METHOD

This chapter presents the details of the validations and verifications carried out on the solution method used for computational simulation. The verification section gives the mesh independent studies on 2D and 3D cavities and the time independent study on the 2D cavity flow. In the validation section the 2D cavity is validated against benchmark computational solutions while the 3D cavity is validated against experimental results cited in the literature.

5.1 Solver Settings for Numerical Simulations.

5.1.1 Discretization of the Solution Domain

The solution domain is discretized for the Finite Volume Method which is based on the control volume formulation. The first step in the discretization is to divide the solution domain into several control volumes, also known as cells, where the variable of interest (ρ, v, T, p) is located at the center of the control volume. For this study the solution domain which is a simple square region for 2D simulation and a simple cube for 3D simulations is discretized using a structured orthogonal mesh. The size and shape of the discretized cell has an impact on the solution. A mesh independent study is necessary therefore, to ensure that the effects of the mesh on the converged solution is under the defined level of uncertainty. The discretized solution domain in two dimensions is presented below in Figure 13.

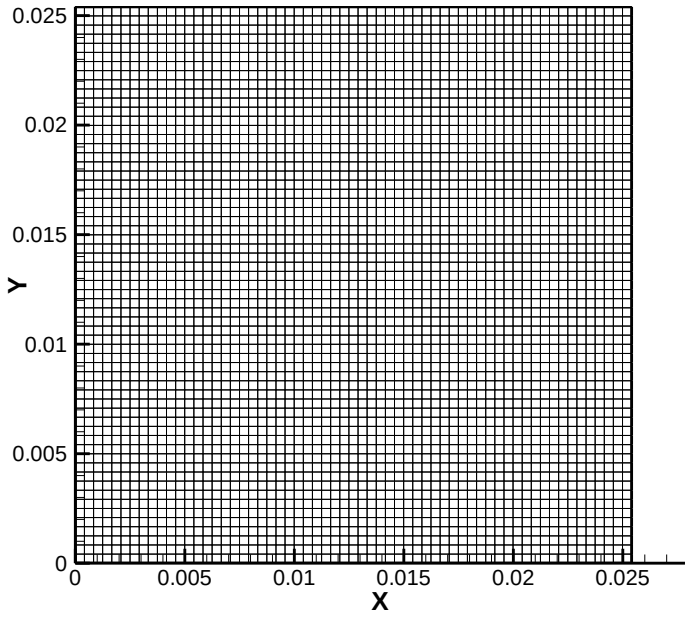

Figure 13 – 61 x 61 Structured Mesh For 2D Simulations

5.1.2 Solver Settings

The pressure-based solver is selected which is ideal for incompressible flows. The viscous model is set to laminar. The solution algorithm is based on the coupled method in which the mass and momentum equation are solved in a coupled fashion. The gradient discretization is Green Gauss cell based. The pressure and momentum discretization are both second order upwind and the residual criteria is set to 1E-10. For unsteady case the temporal discretization is set to second order implicit. For High Reynolds Number the Reynolds Average Navier Stokes Equation is solved with the K-Epsilon turbulence model. The K-Epsilon turbulence model is the model of choice for a wide range of fluid flow applications. Setting up the model itself involves a lot of different parameters to be adjusted. This study uses the standard version of the model with standard wall functions. These wall functions are physics based or empirically developed to cater the viscous effects near the wall. The two-transport equation for the turbulent kinetic energy and the dissipation rate are solved using the second order upwind method. All the CFD settings for steady and unsteady simulation settings are presented in Table 5, Table 6 and Table 7.

Table 6 – CFD Solver settings for Steady State, Low Reynolds Number (laminar) Flows

CFD SOLVER SETTINGS	
Description	**Settings**
Solver	Pressure Based
Viscous	Laminar
Pressure – Velocity Coupling	Coupled
Gradient Discretization	Green Gauss Cell Based
Pressure Discretization	Second Order Upwind
Momentum Discretization	Second Order Upwind
Residual Criteria	1E-10

Table 7 – CFD Solver settings for Unsteady Flows

CFD SOLVER SETTINGS	
Description	**Settings**
Solver	Pressure Based
Time	Transient
Viscous	Laminar
Pressure – Velocity Coupling	Coupled
Gradient Discretization	Green Gauss Cell Based
Pressure Discretization	Second Order Upwind
Momentum Discretization	Second Order Upwind
Transient Formulation	Second Order Implicit
Residual Criteria	1E-10

Table 8 – Solver Settings for Steady State, turbulent flows.

K-Epsilon Turbulence Model Settings	
Description	**Settings**
Turbulence Model	K Epsilon
No of Equations	2
Model Type	Standard
Near Wall Treatment	Standard Wall Function
Turbulent Kinetic Energy Discretization	Second Order Upwind
Turbulent Dissipation Rate	Second Order Upwind
Cmu (Model Constant)	0.01
C1 – Epsilon (Model Constant)	1.44
C2 – Epsilon (Model Constant)	1.92
TKE Prandtl Number (Model Constant)	1
TDR Prandtl Number (Model Constant)	1.3

5.2 Verification of the Numerical Method

The verification of the numerical method is carried out using the mesh independence study and time independence study. The mesh independence study is performed on both 2D and 3D cavity domains and the time independence study is performed on the 2D cavity flow domain using the solver settings tabulated in Table 5.

5.2.1 Mesh Independence Study on the 2D mesh.

The mesh independence study is used to analyze the effect the mesh size has on the converged solution. The study is carried out by keeping all the solver settings same for each run and only changing the mesh size. The horizontal and vertical velocity profiles on the horizontal and vertical centerline are observed for the difference in shape of their profile (if any) or the magnitudes at the peak value for the changes in the mesh size. This study is carried out at Reynolds Number of 1000 at steady state conditions and the results are presented in Figure 14 and 15 and summarized in Table 8

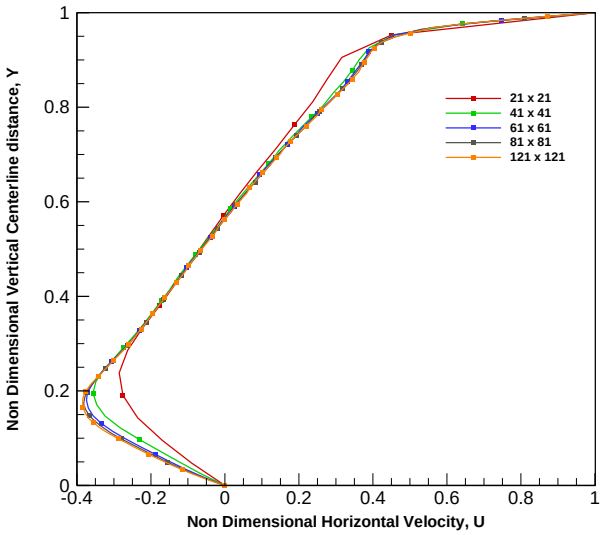

Figure 14 – Non-Dimensional Horizontal Velocity, U on the Vertical Centerline of the cavity for different mesh sizes at Re=1000

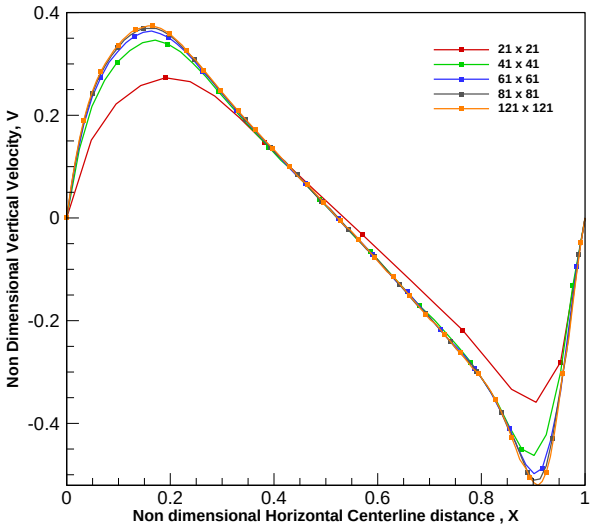

Figure 15 – Non-Dimensional Vertical Velocity, V on the horizontal Centerline of the cavity for different mesh sizes at Re=1000

Table 9 – Summary of the results of the mesh independence study carried out on 2D cavity at Re=1000.

	Grid Size				
	21 x 21	41 x 41	61 x 61	81 x 81	121 x 121
Maximum u	0.0396	0.0396	0.0396	0.0396	0.0396
Minimum u	-0.0113	-0.0141	-0.0148	-0.0151	-0.0152
Maximum v	0.0108	0.0136	0.0144	0.0146	0.0148
Minimum v	0	0	0	0	0

5.2.2 Mesh Independence Study on the 3D mesh.

Unlike 2D, the 3D simulations are more complex and involves the z-momentum equation. This raise the need to conduct a separate mesh independence study for 3D flow domain. It can be observed from the results that changing the mesh in 3D produces a much more significant effect on the converged solution compared to 2D flow domain. Choosing the correct mesh size so that the uncertainty stays minimum is very important in 3D simulations. The results of the mesh independence study in 3D are presented in Figures 16 and Figure 17 and summarized in Table 10.

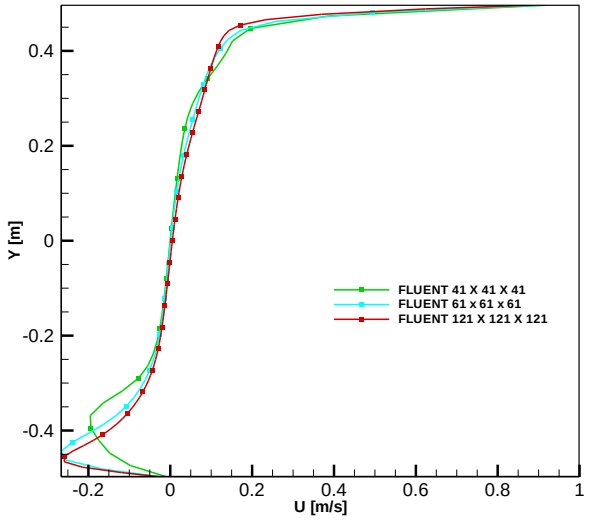

Figure 16 – Non-Dimensional Horizontal Velocity, U on the Vertical Centerline of the cavity simulated in 3D for different mesh sizes at Re=3200

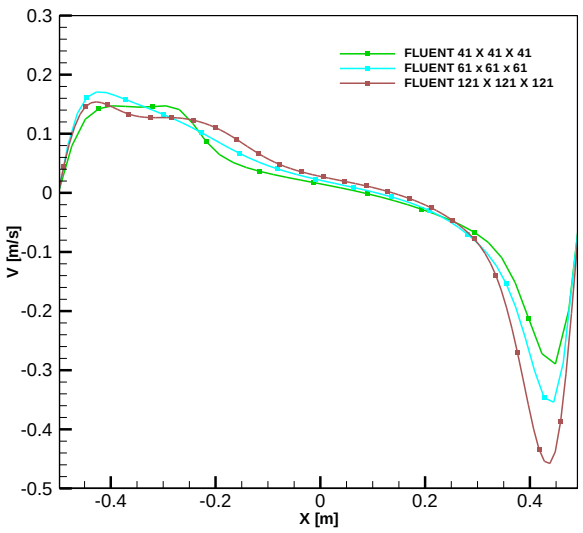

Figure 17 – Non-Dimensional Vertical Velocity, V on the Vertical Centerline of the cavity simulated in 3D for different mesh sizes at Re=3200

Table 10 – Summary of the results of the mesh independence study carried out on 3D cavity at Re=3200

	Grid Size		
	41x41x41	61x61x61	121x121x121
Non-Dim U_{min}	-0.1850	-0.2280	-0.2250
Non-Dim U_{max}	1.000	1.000	1.000
Non-Dim V_{min}	-0.2400	-0.3500	-0.4450
Non-Dim V_{max}	0.1400	0.1750	0.1450

5.2.3 Verification of Half Domain Simulations Using Symmetry Boundary Conditions.

The commercial solver package gives the option of simulating half domain instead of the full domain by providing an option called the symmetry boundary condition. This saves both time and computational cost. For problems like 3D cavity which's geometry is naturally symmetric, the symmetry boundary condition can be effectively used with high accuracy. A separate verification is carried out by comparing results from symmetry boundary condition and full domain simulations. The result is summarized in Table 11 and presented Figure 18.

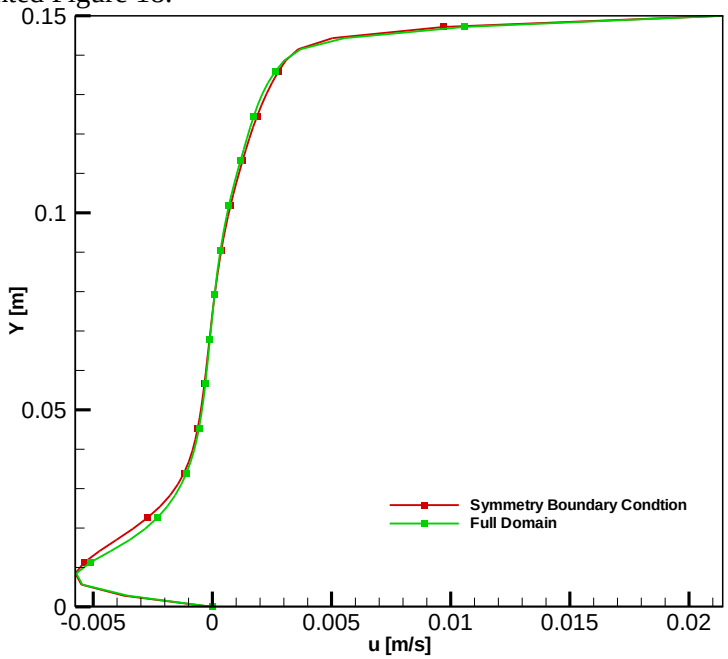

Figure 18 – Horizontal Velocity, U on the Vertical Centerline of the cavity simulated in 3D for full domain and symmetry boundary conditions at Re=3200

Table 11 – Verification of Half Symmetry Domain at Re=3200

	Symmetry	**Full Domain**
Min U [m/s]	-0.0057	-0.0056

5.2.4 Time Independence Study for Unsteady Lid Driven Cavity Flow

A time independent study is also carried out but unlike the mesh independence study discussed in section 5.2.2, the time independent study is carried out at unsteady state conditions in which the temporal term is solved numerically using a second order implicit formulation. In contrary to the mesh independence study, the mesh along with the other solver settings are kept the same for each case, however the time step is increased from small to large. The total time of the simulation is kept constant. That is to say that if the simulation is to be run for 10 seconds with a time step of 0.1 seconds, then the number of steps is kept at 100 while at a time step of 0.2 seconds the number of steps is kept at 50. The number of iterations at each time step are also kept the same for each run. The parameters investigated for the time independent study are the horizontal and vertical velocities on the vertical and horizontal centerline of the 2-dimensional cavity. Also, the velocity at a point near the upper right corner of the lid are studied as well. The results of the time independence study are presented in Figure 19, 20 and 21

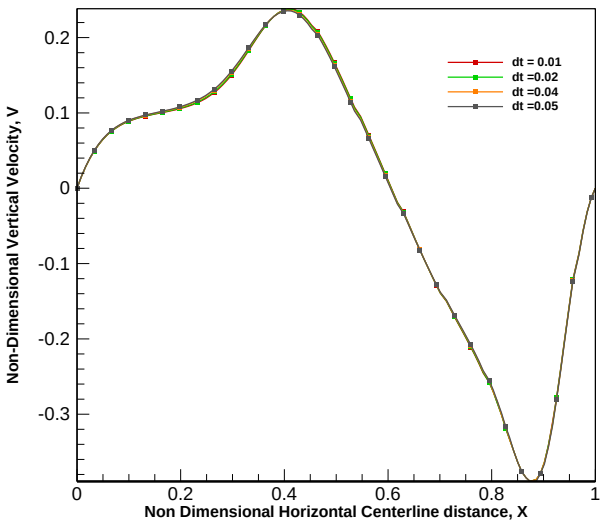

Figure 19- Non-Dimensional Vertical Velocity V on the Horizontal Centerline for different time steps Re=1000

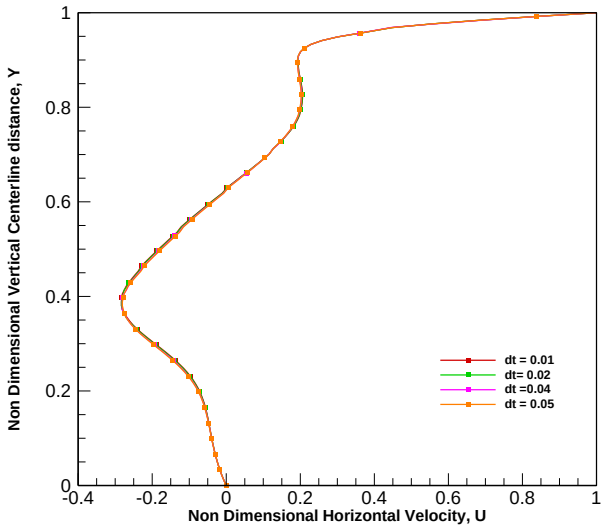

Figure 20 - Non-Dimensional Vertical Velocity U on the Vertical Centerline for different time steps at time, t=5sec and Re=1000

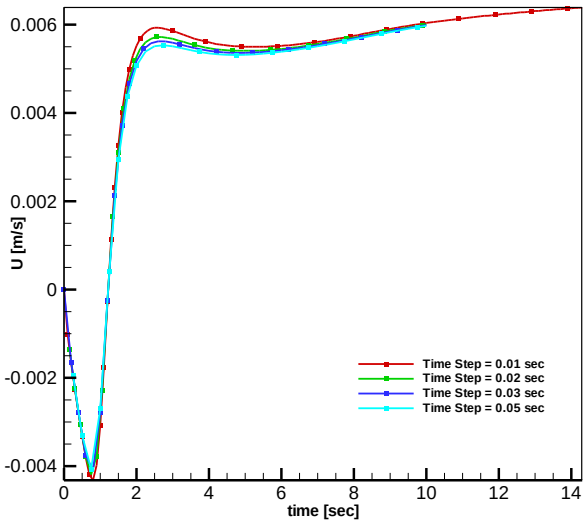

Figure 21- U Velocity profiles at point X = 0.020, Y = 0.021m at Re=1000

Table 12 – Results of U velocity profiles at point X = 0.020 & Y =0.021 for unsteady case at Re=1000

Time Increment Per Step				
	t=0.01	t=0.02	t=0.04	t=0.05
Maximum u [m/s]	0.00639	0.00601	0.00599	0.00597

5.3 Validation:

The validation study is performed for laminar and turbulent flow regimes separately from sources cited in open literature. For laminar simulations Ghia et al [9] is used as benchmark solution while for turbulent flows, results from the experiments performed by Koseff [3] are used.

5.3.1 Validation of the Numerical Simulation Results with Benchmark Computational Solutions for Laminar Flows.

A numerical code that solves the mathematical model, which in this case is the system of governing partial differential equation; continuity, x-momentum, y-momentum & z-momentum equation (for 3D simulations) uses a finite volume technique which is second order implicit in time and space. To establish the validity of the code a standard practice is to run the code on a standard fluid flow case study and compare the results with benchmark solutions available in the literature. Here the results from the commercial solver package are compared with Ghia et al. on the 2-D cavity of Aspect Ratio 1. The comparison is made for low Reynolds number in the laminar flow regime and the results are shown below: One can easily see that that results from the commercial solver agrees with that of Ghia at al. for all Reynolds number in the laminar flow range. However, as the flow start to transition into turbulence there happens to be disagreements in the magnitudes of the U velocities near the bottom of the cavity. A comparison at Re 5000 suggests that the laminar model can no longer be used to predict flow characteristics at this Reynolds Number and beyond. A possible reason could be that neither FLUENT nor GHIA considers the fluctuations in velocity due to turbulence. From the validation study of numerical simulations of laminar case (From Figure 22 to Figure 27) it can be observed that the results made good

agreement with the benchmark solution. However, as the Reynolds Number increased, the numerical predictions made from the commercial solver underestimated the benchmark solution velocity magnitudes. At Re 5000 the degree of dissimilarity between the velocity distributions obtained on the vertical and horizontal centerlines and the velocity magnitudes benchmark computational solution is the greatest. It can thus be deduced that the benchmark numerical solution of Ghia et al. is not suitable for comparison at high Reynolds numbers (Turbulent Flows). This argument can further be strengthened from the fact that by the application of turbulence models the effects of eddy viscosity would further lower the velocity magnitude from the laminar flow case making the disparity between the velocity distributions of benchmark numerical solutions and commercial package increase even more. All these results are summarized in Table 13.

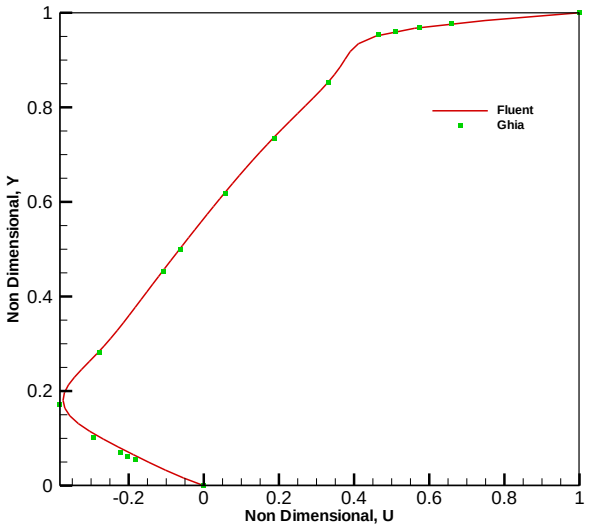

Figure 22-Non-Dimensional Horizontal Velocity, U on the Vertical Centerline for Re=1000

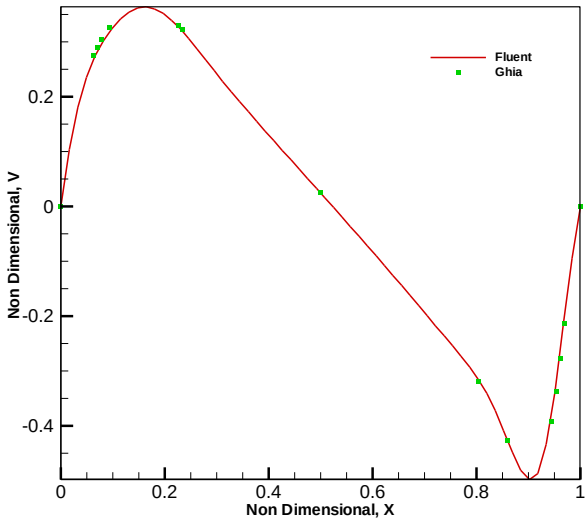

Figure 23-Non-Dimensional Vertical Velocity V, on the horizontal Centerline for Re=1000

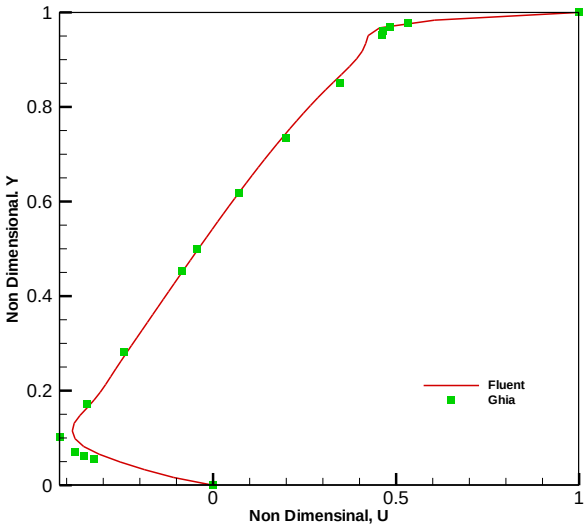

Figure 24-Non-Dimensional Horizontal Velocity, U on the Vertical Centerline for Re=3200

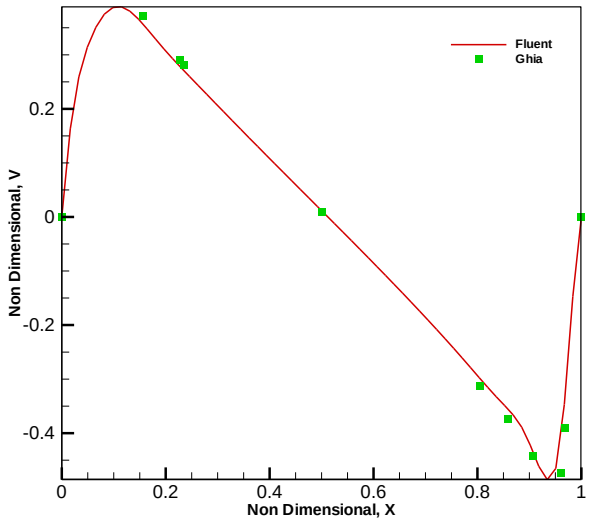

Figure 25-Non-Dimensional Vertical Velocity V, on the horizontal Centerline for Re=3200

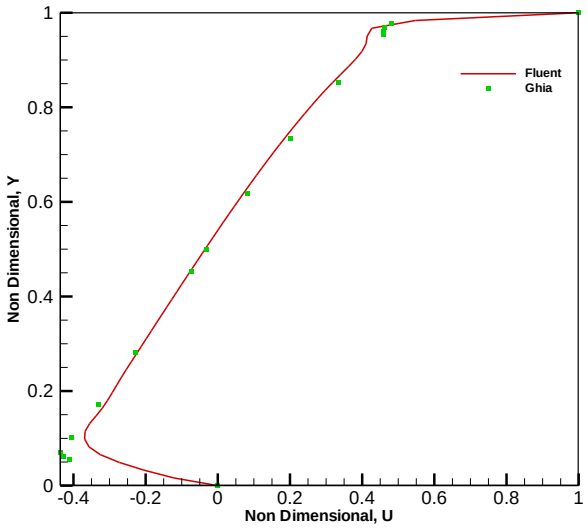

Figure 26-Non-Dimensional Horizontal Velocity U on the Vertical Centerline for at Re=5000

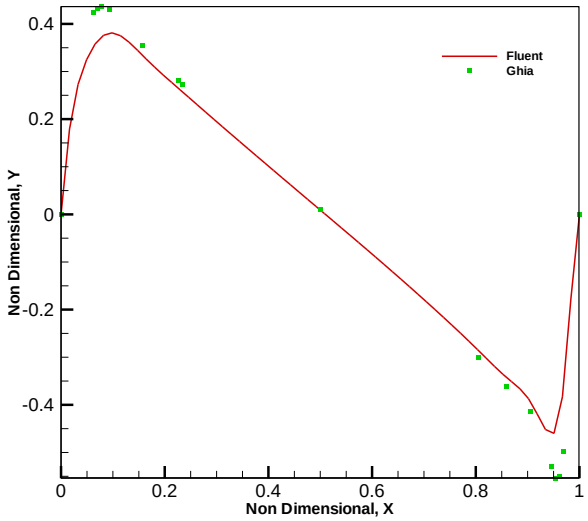

Figure 27-Non-Dimensional Vertical Velocity V, on the Horizontal Centerline at Re=5000

Table 13 – Summary of Results of the validation Study at Low Reynolds Number

Results				
		FLUENT	GHIA	% Dev
Re 1000	Min U	-0.3744	-0.38289	2%
	Max U	1.0000	1.0000	0%
	Min V	-0.4980	-0.5155	3%
	Max V	0.36400	0.37095	2%
Re 3200	Min U	-0.3844	-0.4194	8%
	Max U	1.0000	1.0000	0%
	Min V	-0.4980	-0.54503	9%
	Max V	0.3888	0.42768	9%
Re 5000	Min U	-0.3690	-0.43643	15%
	Max U	1.0000	1.0000	0%
	Min V	-0.4980	-0.5541	10%
	Max V	0.3812	0.43648	13%

5.3.2 Validation of the Numerical Simulation Results with Experimental results from the literature for Turbulent Flows.

As discussed earlier that the benchmark numerical solution for the lid driven cavity flow problem which has been effective for validating computational simulations in laminar flow regime is not as effective and reliable for turbulent flows. For turbulent flows, experiments from Koseff [3] were identified in the published literature in the experimental lid driven cavity flow problem to work better for validation. In this section, for high Reynolds Number, the RANS equation has been solved numerically using the commercial solver. The K Epsilon turbulence closure model is the model of choice for all simulations in turbulent flow regime in this thesis. The experimental results are dominated by the 3D nature of the flow fields. The validation is thus performed by simulation in the 3D cavity. The results of the validation study indicate that the K Epsilon model is a good predictor for turbulent flows. The k Epsilon model with standard wall functions fares well at both transition and fully turbulent experimental results. In Figure 28 and 29, at Re 5000 the CFD predictions using K Epsilon agrees with the experimental results however slight underestimation can be observed in the U velocity distribution on the vertical centerline of the cavity near the bottom stationary wall. A similar trend is observed at Re 7500. It can be seen in Figure 30 and Figure 31 that the CFD predicted velocity distributions are offset to the experimental dots near the walls but comes near at the center of the cavity.

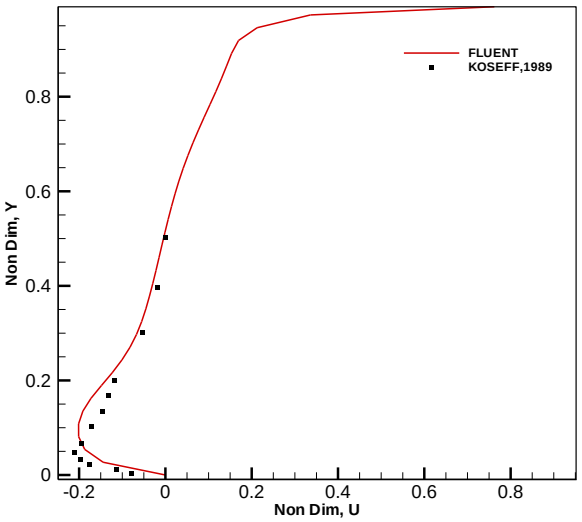

Figure 28- Non-Dimensional U velocity on vertical Centerline of the center plane of 3D cavity for Re= 5000

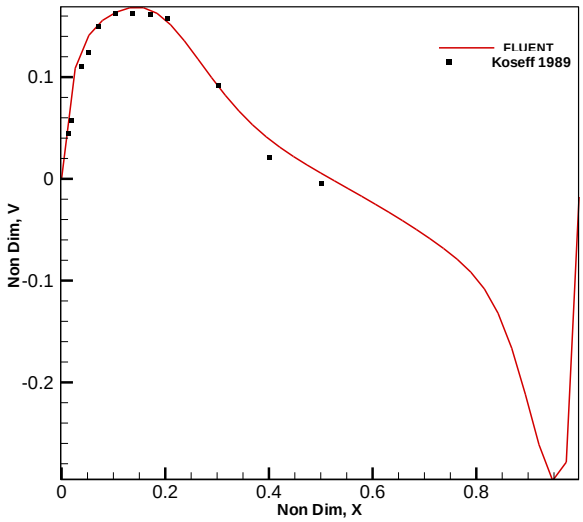

Figure 29- Non-Dimensional V velocity on horizontal Centerline of the center plane of 3D cavity for Re=5000

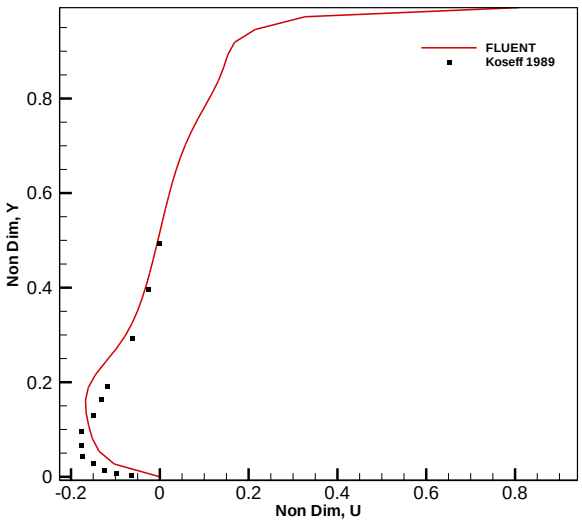

Figure 30- Non-Dimensional U velocity on vertical Centerline of the center plane of 3D cavity for Re=7500

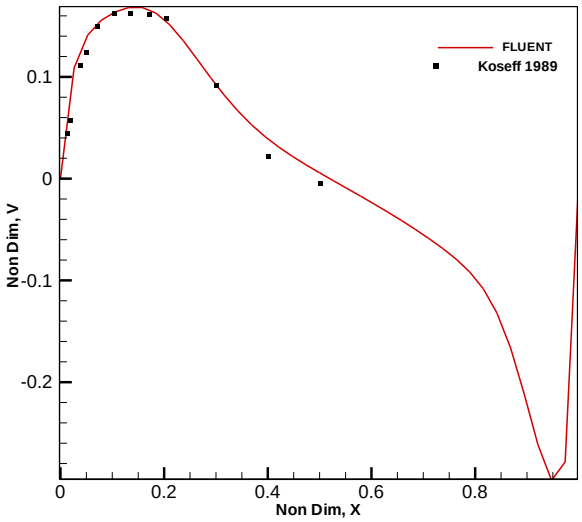

Figure 31- Non-Dimensional V velocity on horizontal Centerline of the center plane of 3D cavity for Re=7500

Table 14 – Summary of Results of the validation Study at High Reynolds Number (Turbulent Flow)

		Results	
		FLUENT (K EPSILON)	KOSEFF 1989
Re 5000	Min U	-0.2013	-0.2101
	Max U	1	-
	Min V	-0.2964	-
	Max V	0.1681	0.1627
Re 7500	Min U	-0.1673	-0.1770
	Max U	1	-
	Min V	-0.2440	-
	Max V	0.1500	0.1354

6. NUMERICAL PREDICTIONS OF LID DRIVEN CAVITY FLOW FOR LAMINAR AND TURBULENT FLOW CASES.

In this chapter the numerical solution method adopted in Chapter 5 is used to make predictions for laminar and turbulent lid driven cavity flows. A calibration study of the turbulence model is also included where a model coefficient is fine tuned for better predictions in the transition and turbulent flow regimes.

6.1 Numerical Predictions for Laminar Flows

Using the solver settings in Table 4, a lid speed of u=0.03956m/s that corresponds to a lid Reynolds number of Re 1000 was simulated. The results are presented in the forms of velocity and pressure contours, vector and streamline plots and the U and V velocity distributions along the vertical and horizontal centerlines in Figure 32 to 35 respectively and summarized in Table 15.

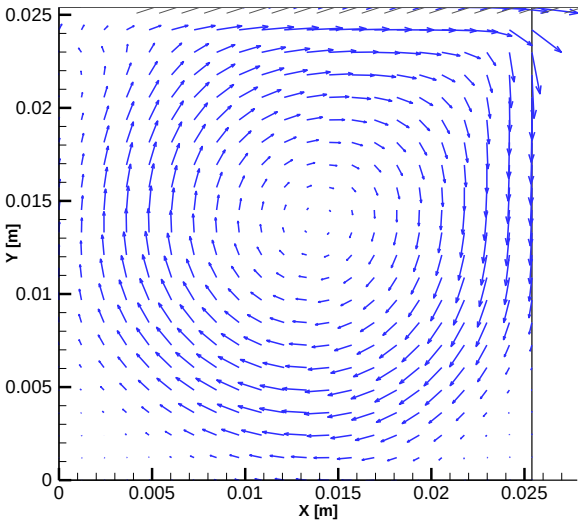

Figure 32- Velocity Vector Plot for Re=1000 at Steady State

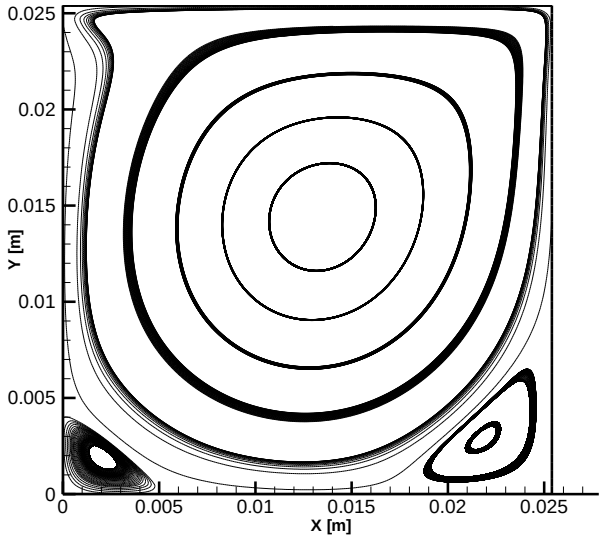

Figure 33- Streamline Plot for Re=1000 at Steady State

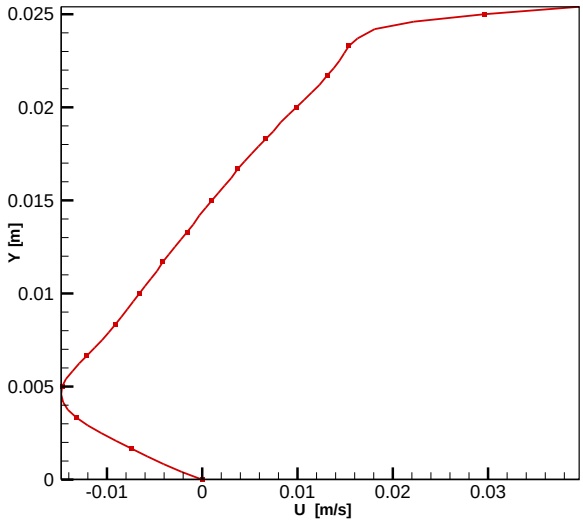

Figure 34- U velocity distribution on the vertical centerline at Steady State for Re=1000

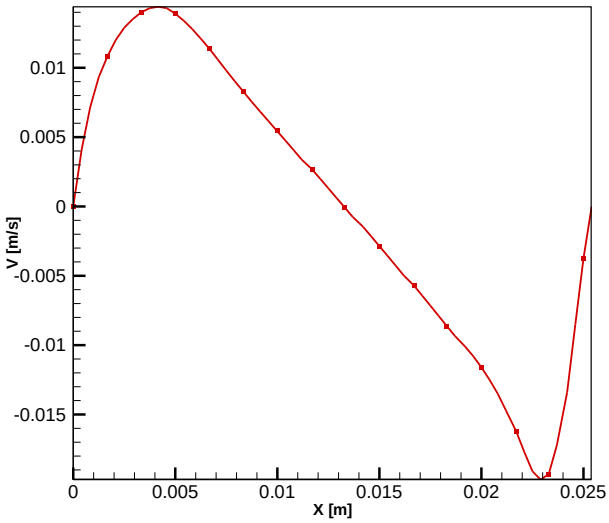

Figure 35- V velocity distribution on the horizontal centerline at Steady State for Re=1000

Table 15 – Summary of Result of the CFD (Fluent) Simulation at Re 1000

Results			
Maximum u [m/s]	Minimum u [m/s]	Maximum v [m/s]	Minimum v [m/s]
0.0396	-0.01483	0.0144	-0.0197

6.2 Calibration of the Turbulence Model.

This section embarks on proposing an approach to find the optimal value of the closure coefficient to improve the accuracy of the simulations for higher Reynolds Numbers. The K Epsilon turbulence model was adapted as the closure model for numerical simulations of the RANS equations in transitional and fully turbulent flows inside the lid driven cavity. The equations numbered (9) to (14) in Chapter 5 presents the unsteady form of the RANS equations together with the K Epsilon closure model. The value of the coefficient of eddy viscosity for the K Epsilon model has a direct influence on the shear stress terms in the RANS equation. By adjusting the model coefficients, the turbulent shear stress can be

enhanced or reduced which in turn will affect velocity magnitudes predicted by the CFD simulation. Velocity distributions along the centerlines predicted by the modified K Epsilon model are compared with the laminar solution at the lower end of the transition region and with the standard K Epsilon turbulence model with standard settings at the upper end of the transition region. The term 'convergence' is used here with repetition to explain that the distributions predicted from the modified K Epsilon is approaching towards the laminar solution. The results of the calibration study are given in Figures 36 to 41 and summarized in Tables 16 and 17. Reynolds number 4000, 4500 and 5000 are simulated using the K Epsilon turbulence model twice. Once with the standard value of the coefficient of eddy viscosity, $C\mu$ and then another time with the adjusted value. The U and V velocity distributions along the vertical and horizontal centerlines respectively from each coefficient value settings are compared with the laminar solution from Figure 36 to Figure 41. Table 16 compares the maximum and minimum velocities along the vertical centerline for laminar, standard K Epsilon and adjusted K Epsilon and gives the percentage deviation as well. At Reynolds number 4500 the difference between the maximum and minimum U velocities between the laminar solution and the adjusted K Epsilon model is the least i.e., 8% at the maximum and 9% at the minimum. A similar trend can be seen in Table 17 which is comparing the V velocities in a similar manner. The percentage deviation between the minimum V velocity is 9% at Re 4500. For all three Reynolds Number simulated it was found that the percentage deviation at the maximum V velocities between laminar solution and K Epsilon based simulation result with reduced $C\mu$ was 21%.

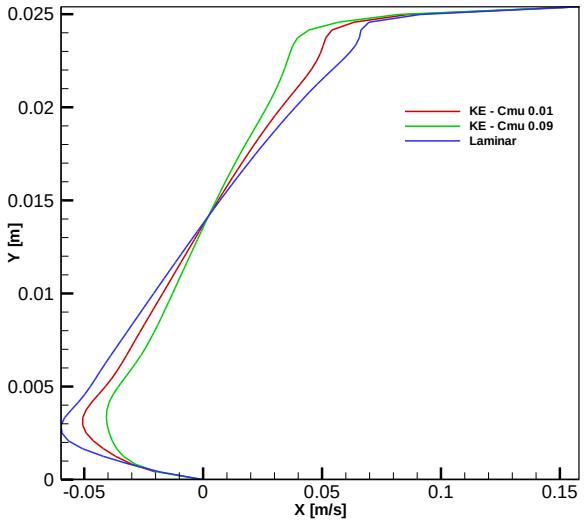

Figure 36 – Comparing U Velocity Profiles on the Vertical Centerline for different Cμ at Re=4000

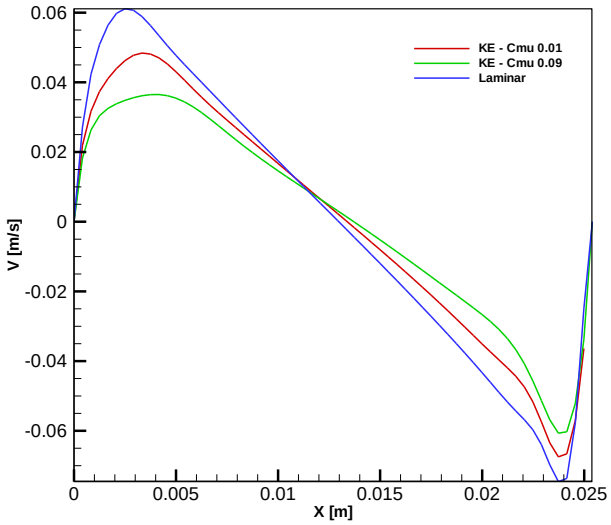

Figure 37 – Comparing V Velocity Profiles on the horizontal Centerline for different Cμ at Re=4000.

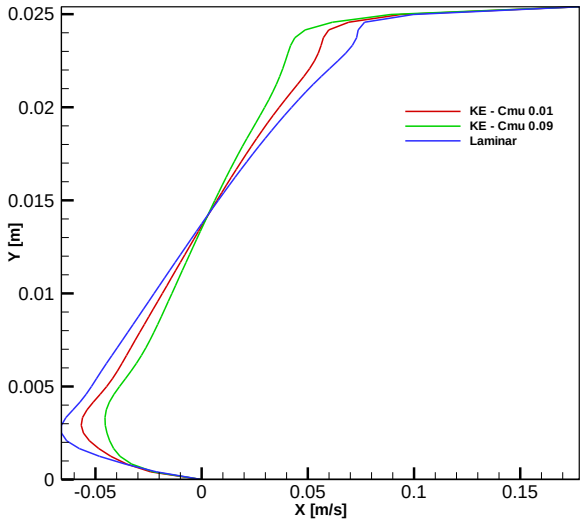

Figure 38 –Comparing U Velocity Profiles on the Vertical Centerline for different Cμ at Re=4500

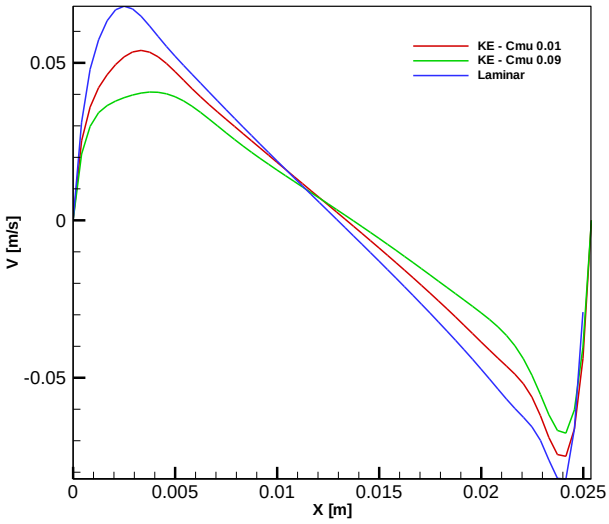

Figure 39 – Comparing V Velocity Profiles on the horizontal Centerline for different Cμ at Re=4500

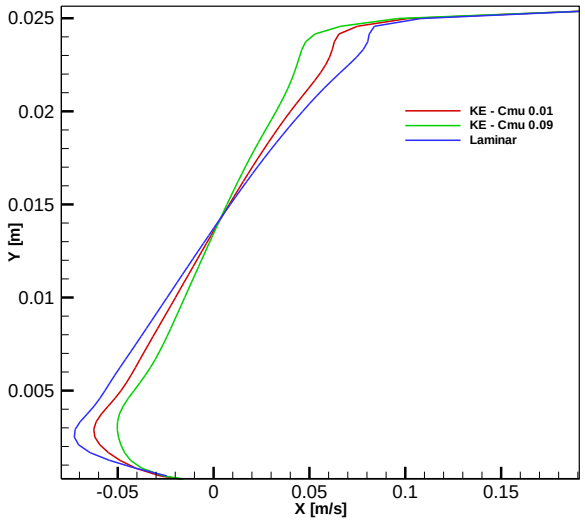

Figure 40 – Comparing U Velocity Profiles on the Vertical Centerline for different Cμ at Re=5000

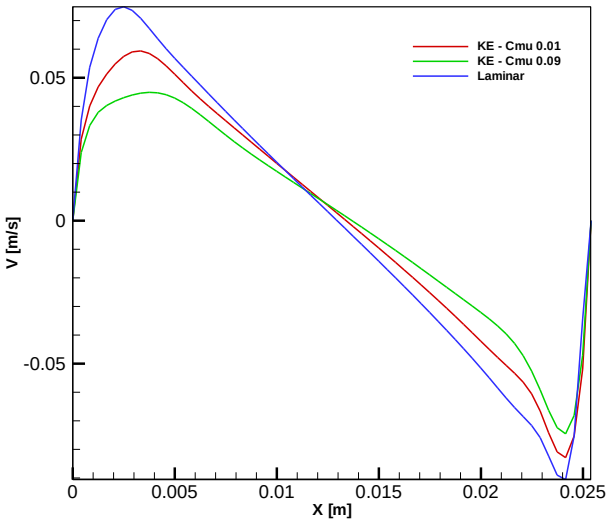

Figure 41 –Comparing V Velocity Profiles on the horizontal Centerline for different Cμ at Re=5000

Table 16 – Comparing Maximum and Minimum U Velocity Values on the Vertical Centerline for different Reynolds numbers between K Epsilon Model with standard Cμ and adjusted (reduced) Cμ.

Re		Laminar	KE- Cμ =0.09	KE- Cμ =0.01	% Dev
	Max U [m/s]	0.0912	0.0820	0.0860	7%
4000	Min U [m/s]	-0.0597	-0.0407	-0.0506	15%
	Max U [m/s]	0.0997	0.0891	0.0912	8%
4500	Min U [m/s]	-0.0661	-0.0455	-0.0597	9%
	Max U [m/s]	0.1978	0.0960	0.1013	49%
5000	Min U [m/s]	-0.0726	-0.0502	-0.0625	14%

Table 17 – Comparing Maximum and Minimum V Velocity Values on the Horizontal Centerline for different Reynolds numbers between K Epsilon Model with standard Cμ and adjusted (reduced) Cμ

Re		Laminar	KE- Cμ =0.09	KE- Cμ =0.01	% Dev
	Max V [m/s]	0.0611	0.0364	0.0484	21%
4000	Min V [m/s]	-0.0745	-0.0607	-0.0674	10%
	Max V [m/s]	0.0679	0.0407	0.0539	21%
4500	Min V [m/s]	-0.0821	-0.0676	-0.0749	9%
	Max V [m/s]	0.0748	0.0449	0.0593	21%
5000	Min V [m/s]	-0.0905	-0.0745	-0.0829	8%

6.3 Numerical Predictions for Turbulent Flows.

The calibrated turbulence model is used to make numerical predictions for turbulent flows. The results are presented below in the form of Turbulent Viscosity Contour Plots and U and V velocity plots on the vertical and horizontal centerlines. Figure 42 to 44 and summaries in Table 18.

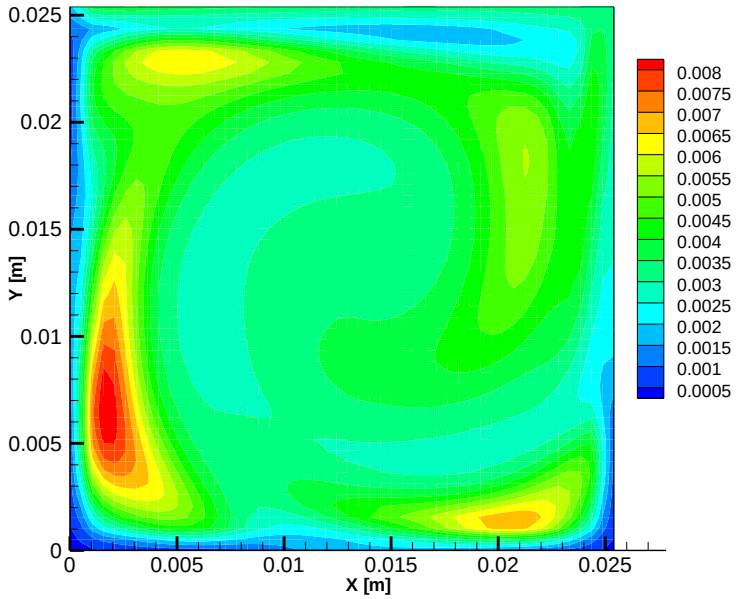

Figure 42- Contour plot of Turbulent Viscosity at Re 10 000 Steady State.

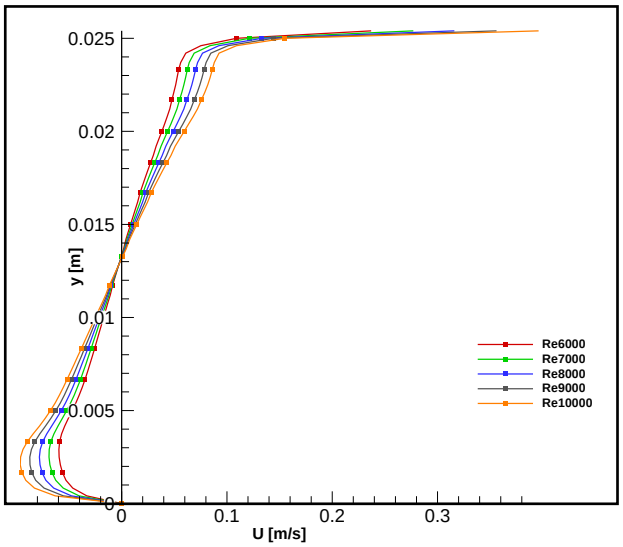

Figure 43- U velocity profile on the vertical centerline for Reynolds Number ranging from 6000 to 10 000

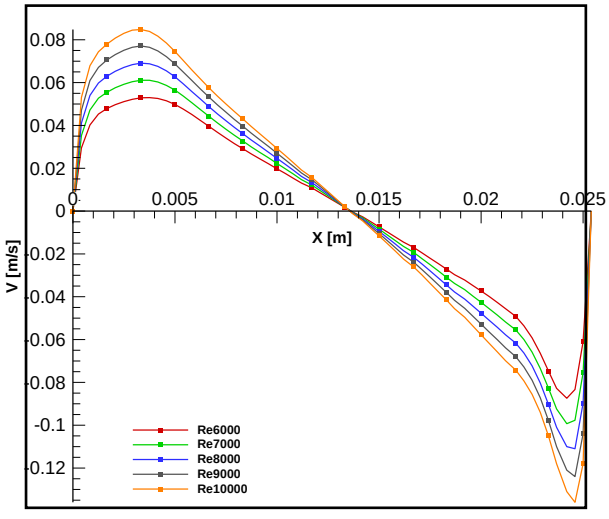

Figure 44- U velocity profile on the vertical centerline for Reynolds Number ranging from 6000 to 10 000

Table 18 – Summary of Results for Steady State Lid Driven Cavity Flow for Higher Reynolds Number using K-Epsilon Turbulence Model

Results				
Reynolds Number	Maximum u [m/s]	Minimum u [m/s]	Maximum v [m/s]	Minimum v [m/s]
6000	0.0396	-0.0148	0.0120	-0.0155
7000	0.2770	-0.0046	0.0138	-0.0199
8000	0.3160	-0.0078	0.0111	-0.0120
9000	0.3560	-0.0089	0.0125	-0.0138
10000	0.3960	-0.0010	0.0139	-0.0157

7. UNSTEADY LID DRIVEN CAVITY FLOW STUDY

In this Chapter the unsteady lid driven cavity flow is numerically simulated for laminar, transition and turbulent flow regimes. The development of the circulation pattern is observed from stagnation to steady state for different Reynolds Number in laminar, transition and turbulent flow regimes. In a separate parametric study, the effect of different lid accelerations on the development of flow is also investigated.

7.1 Development of Circulation Patterns

Most of the studies in the domain of the lid driven cavity flow are concerned with the steady state flow. The thrust of this study is to investigate the unsteady process of the lid driven cavity flow that is the flow approaching the steady state in response to a sudden start of the top lid. The purpose is to capture the time dependent flow fields. A parametric study was conducted to determine the effect of the lid speed on the formation, strength and positional changes of the circulation patterns as the lid driven flow develops from stagnation to steady state. This parametric study covers Reynolds Numbers from 1000 up to 10000. The Reynolds number is determined from the lid speed recorded from the camcorder as discussed in Chapter 3. Figure 45 to 50 shows the development of the circulation patterns in the form of vector plots. These vector plots at various flow times are obtained from the unsteady simulation runs using the commercial solver. The vector plots are clearly showing how the flow is getting developed from stagnation to steady state. A small circulation patter is visible at the top right corner of Figure 45 at time t= 1.0 sec. This circulation grows and moves until the center of the circulation comes close to the geometric center of the cavity where it stabilizes as the flow becomes steady state at time, t = 6.0 sec in Figure 51. Tracing the movement of the center of these primary circulations brought to surface some useful information about the development of the flow which are further discussed in the next paragraph.

From Figure 51, it can be observed that the center of the primary circulation is a function of the Reynolds Number. As the Reynolds Number increases from 6000 to 10,000 the center of the circulation moves

towards the upper right section of the cavity. In Figure, 52 and 53 the development of the circulation pattern is traced from stagnation to steady state. To obtain these simulations the commercial package is set to solve the unsteady laminar model for low Reynolds Number and unsteady RANS model with K - Epsilon closure model for high Reynolds number i.e. Re 5000 and above. The solver settings are explained in chapter 4. The reader can refer to Chapter 4 and see Table 7 for the settings used to run an unsteady simulation. For laminar flow the primary vortex develops at the top right corner of the cavity as soon as the lid begins to move. The vortex moves down following a smooth curvature to settle at a point that is very near to the geometric center of the cavity. The point where the center settles down changes slightly as the Reynolds number is increased, mostly moving in the upward direction i.e. towards the lid. It can be observed in Figure 51 that up to a Reynolds Number of Re 3000, the center of the primary circulation follows an identical path with slight variation. However, when the Reynolds number reaches Re 4000 there can be observed a significant movement of the primary circulation. In Figure 53 it can be observed that for Re 4000 and higher the center of the primary circulation follows a loop before it settles down near to the geometric center of the cavity when the flow becomes steady.

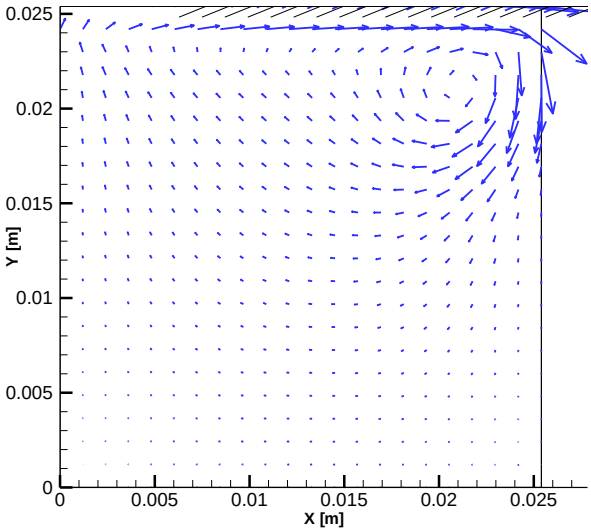

Figure 45 – Velocity Vector Plot at t=1.0 sec for Re=2000

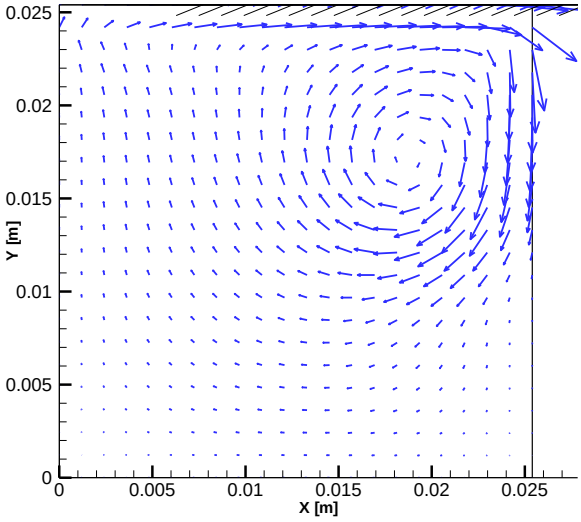

Figure 46 – Velocity Vector Plot at t=2.1 sec for Re=2000

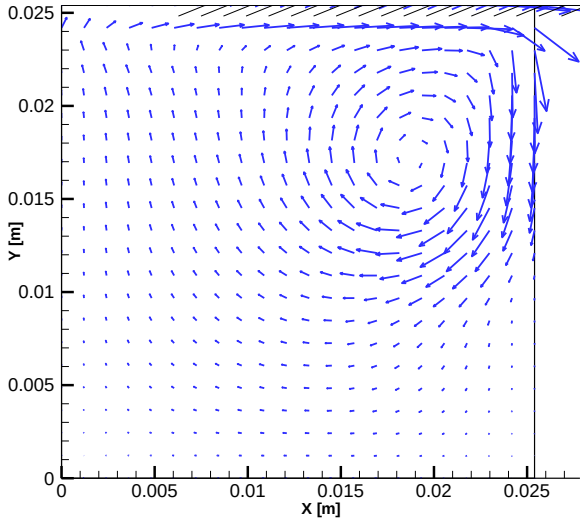

Figure 47- Velocity Vector Plot at t=3.1 sec for Re=2000.

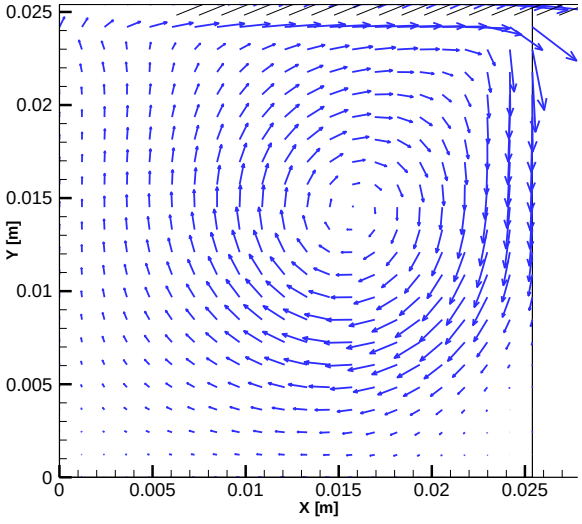

Figure 48- Velocity Vector Plot at t=4.1 sec for Re=2000

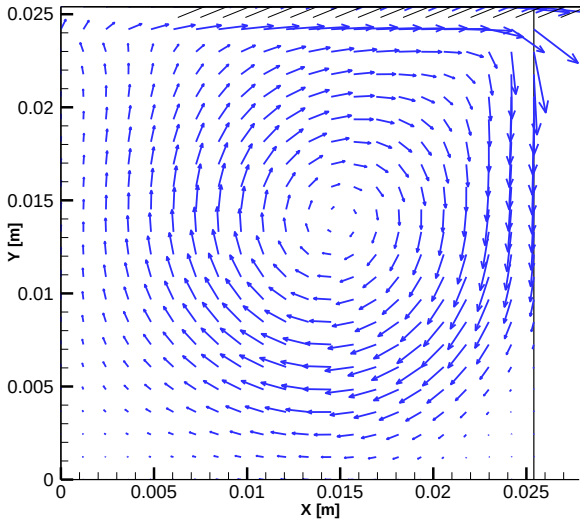

Figure 49 – Velocity Vector Plot at t=5.1 sec for Re=2000.

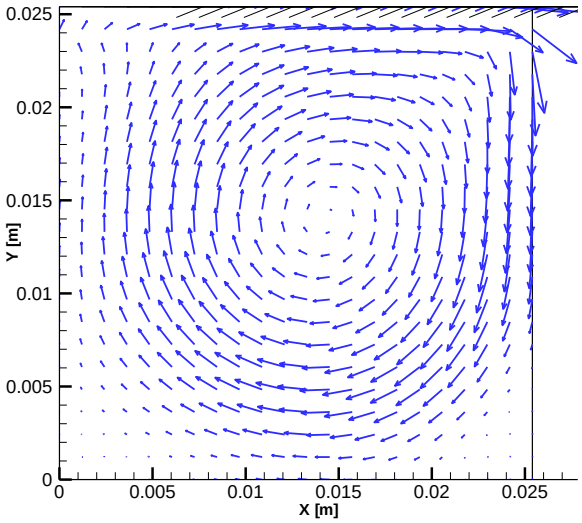

Figure 50 – Velocity Vector Plot at t=6.0 sec for Re=2000.

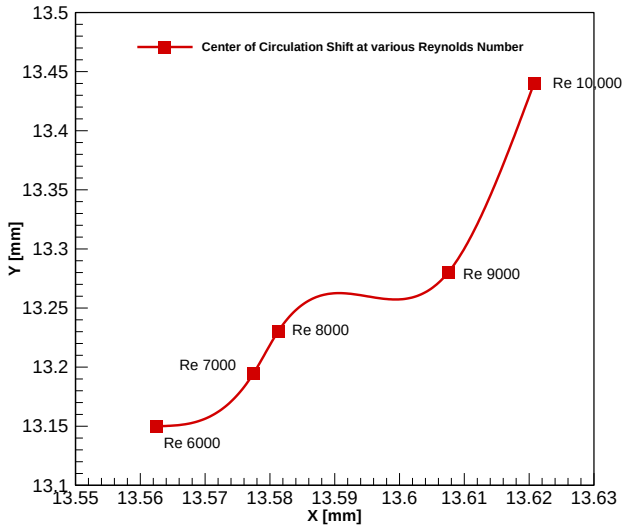

Figure 51 – Center of Circulation for different Reynolds Number at Steady State

Table 19 – Center of Primary Circulation at steady state for different Reynolds Numbers

Results		
Reynolds Number	X [m]	Y [m]
6000	0.01363	0.13440
7000	0.01360	0.13280
8000	0.01358	0.13230
9000	0.01358	0.13120
10 000	0.01356	0.13152

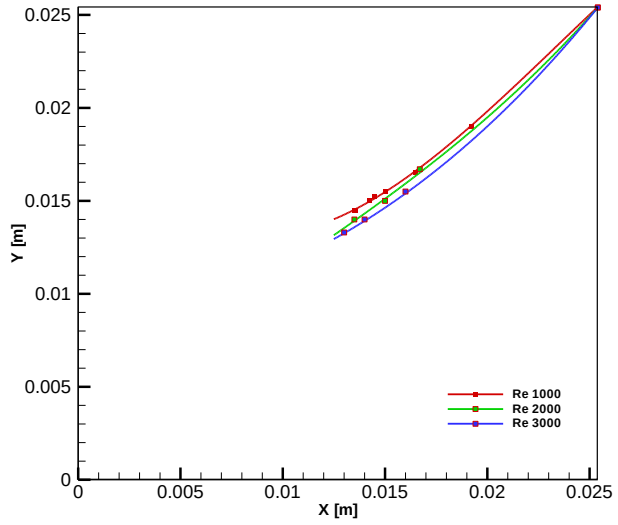

Figure 52 – Path of the Circulation Center from stagnation (beginning) to the end (Steady State) for Reynold Numbers 1000, 2000 and 3000

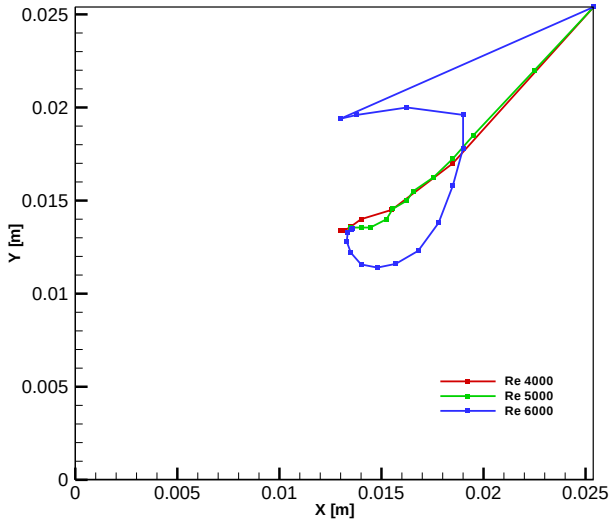

Figure 53 – Path of the Circulation Center from stagnation (beginning) to the end (Steady State) for different Reynold Numbers 4000,5000,6000

7.2 Effect of Lid Acceleration on the Flow Patterns

When the boundary condition on the moving lid is set to a certain lid speed for unsteady simulation in laminar and turbulent regime it was noticed that that the solver ramps up to that speed at an infinitesimally small time. This is contrary to how it works in real practice especially for the case of the experimental setup that this thesis study is using. In the experimental setup shown in Chapter 3, the lid is

moved via a specially designed cavity driver that is powered by a motor driven pulley. To adjust the speed of motor a potentiometer is installed on to the pulley. This potentiometer is meant for reducing or increasing the lid speed according to the experimental plan. When the motor is turned on after the potentiometer knob is rotated a certain angle. The lid ramps up to its maximum speed with a time delay that can be mathematically represented by a sinusoidal delay function. Different forms of lid initiations were tried, and this section gives the results in the form of velocity plots for all those different trials. From Figure 55 to 59 a changing linear lid delay time was induced into the boundary condition. The results however showed that there was not much of a difference between the velocity profiles except that they were offset from one another with a distance that was equal to the time delay set initially. From Figure 59 to 64 the linear and sinusoidal lid time delays are compared for U and V velocity distributions on the vertical and horizontal centerline respectively for various time steps during the development of the flow. The results are also summarized in Table 21. It was observed from the plots that both linear and sinusoidal lid accelerations did not have much difference between them, however as the flow develops the velocity distributions due the sinusoidal lid acceleration has higher velocity peaks and much sharper velocity gradients. Also, it can be inferred that as the flow develops the maximum and minimum velocity values are greater for sinusoidal then linear. Figure 65 to Figure 68 compares the development of the flow from stagnation to steady state for sinusoidal, linear and step lid accelerations and finds that the lid acceleration as a step function produces much more sharper gradients then the others with greater peak values of U and V velocities. These results are also summarized in Table 20.

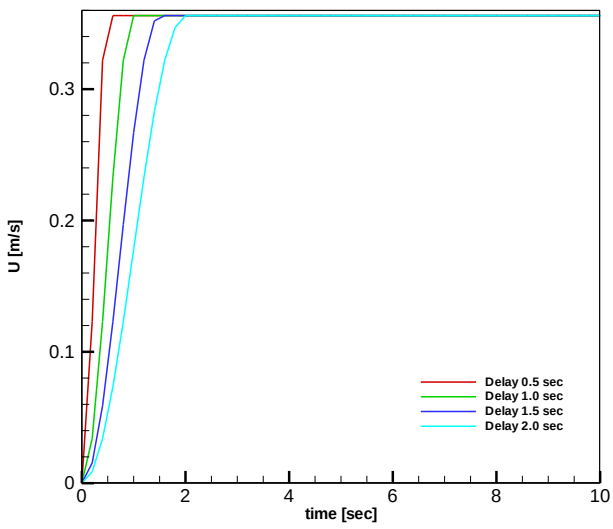

Figure 54- Lid Velocity Profiles for different time delays

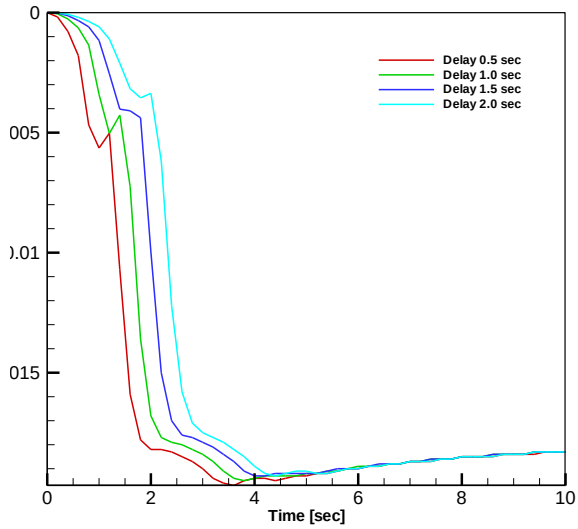

Figure 55 Horizonal Velocity, U variation with time at the point X = 0.0127 & Y=0.0127 for different lid accelerations obtained by changing the lid time delay.

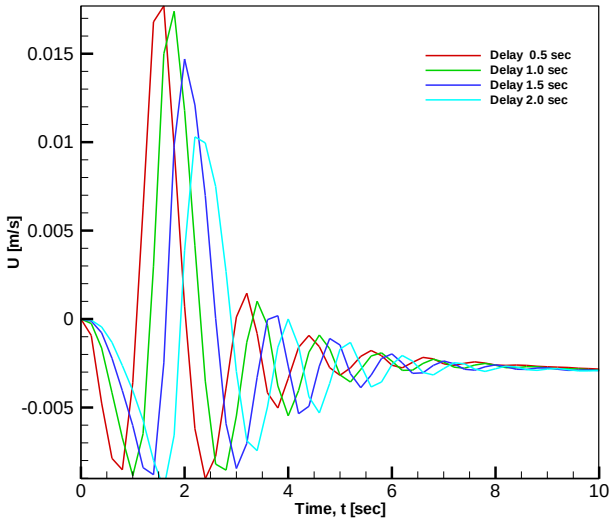

Figure 56- Horizonal Velocity, U variation with time at the point X = 0.002 & Y=0.002 for different lid accelerations obtained by changing the lid time

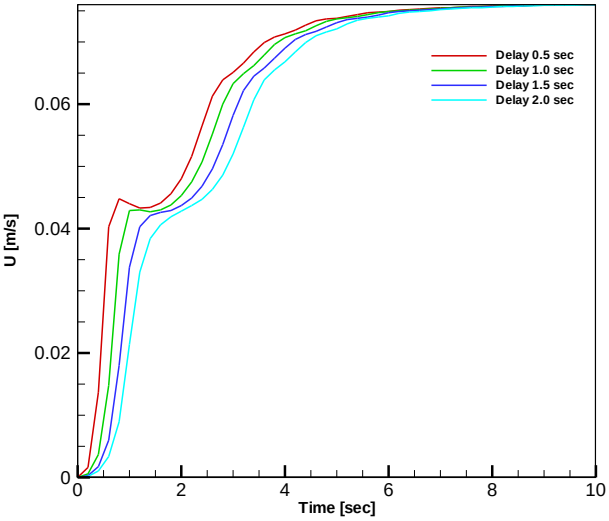

Figure 57- Horizonal Velocity, U variation with time at the point X = 0.022 & Y=0.002 for different lid accelerations obtained by changing

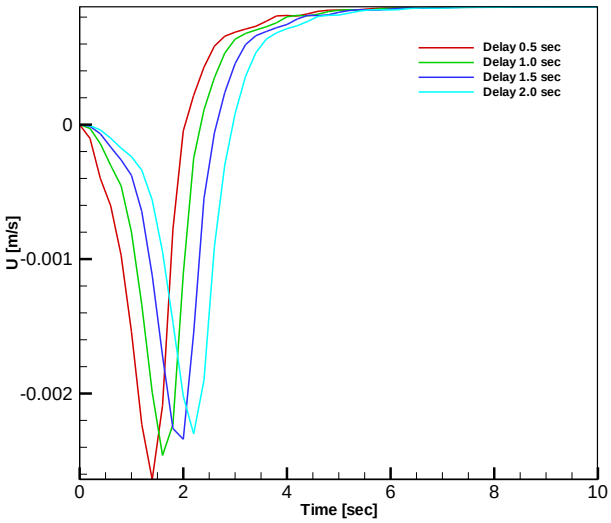

Figure 58- Horizonal Velocity, U variation with time at the point X = 0.020 & Y=0.024 for different lid accelerations obtained by changing the lid time delay.

Table 20 -Comparing Peak U Velocity Values at different point for increasing lid time delay.

Position		**Lid Delay 0.5 sec**	**Lid Delay 1.0 sec**	**Lid Delay 1.5 sec**	**Lid Delay 2.0 sec**
Lid (X=0.0127, Y=0.0254)	U_{max} [m/s]	0.3956	0.3956	0.3956	0.3956
	Time [sec]	0.5	1.0	1.5	2.0
Center (X=0.0127, Y=0.0127)	U_{max} [m/s]	0.0177	0.0174	0.0147	0.0103
	Time [sec]	1.6	1.8	2.0	2.2
Near Lid (X=0.020, Y=0.024)	U_{max} [m/s]	0.076	0.076	0.076	0.076
	Time [sec]	9.4	12.2	12.2	12.2
Bottom Left (X=0.002, Y=0.002)	U_{min} [m/s]	-0.00264	-0.00246	-0.00234	-0.00203
	Time [sec]	1.4	1.6	2.0	2.2
Bottom Right (X=0.022, Y=0.002)	U_{min} [m/s]	-0.0197	-0.0195	-0.0193	-0.0193
	Time [sec]	3.6	3.8	4.0	4.0

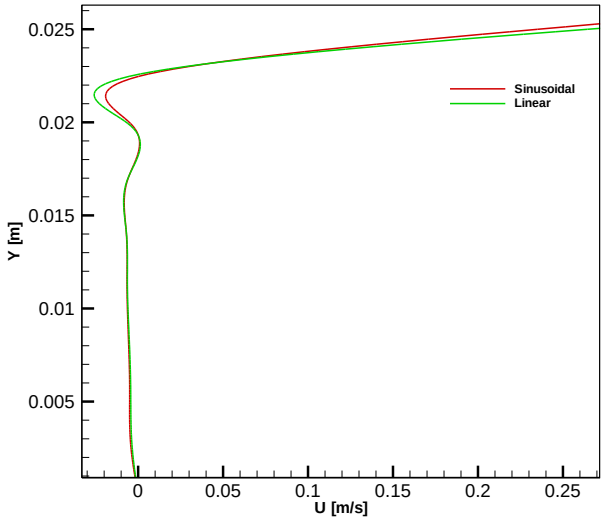

Figure 59-U velocity distribution on the vertical centerline at t=0.8 sec at Re=10 000 for Sinusoidal and linear lid time delays.

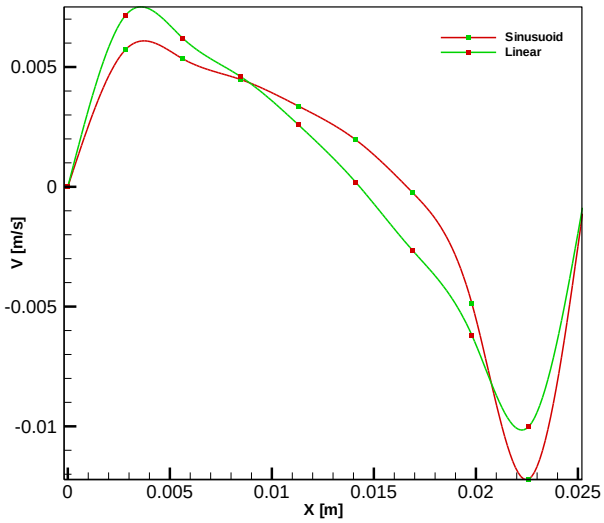

Figure 60-V velocity distribution on the horizontal centerline at t=0.8 sec at Re=10 000 for Sinusoidal and linear lid time delays.

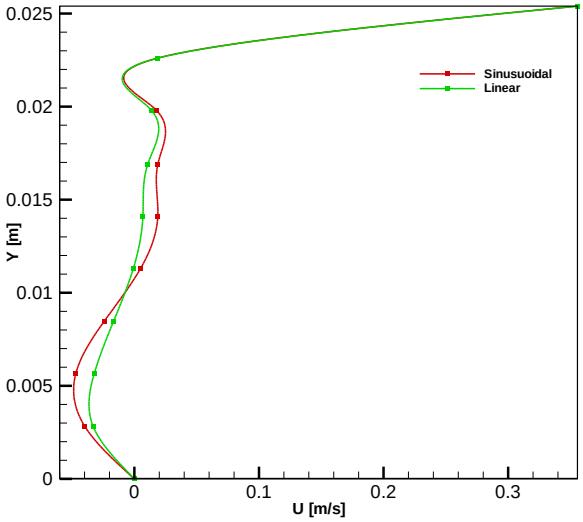

Figure 61-U velocity distribution on the vertical centerline at t=1.6 sec at Re=10 000 for Sinusoidal and linear lid time delays.

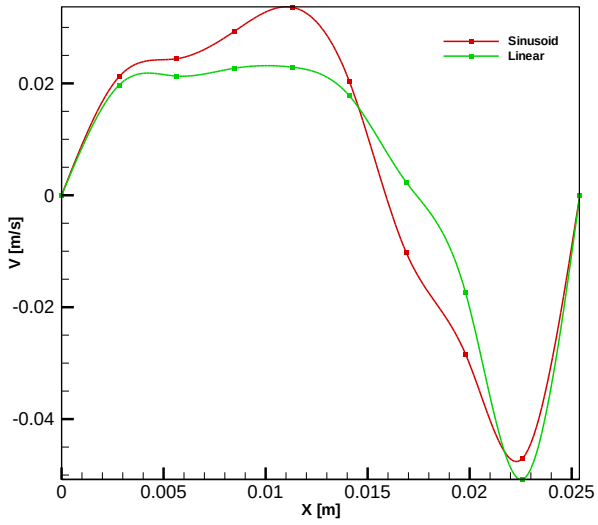

Figure 62-V velocity distribution on the horizontal centerline at t=1.6 sec at Re=10 000 for Sinusoidal and linear lid time delays.

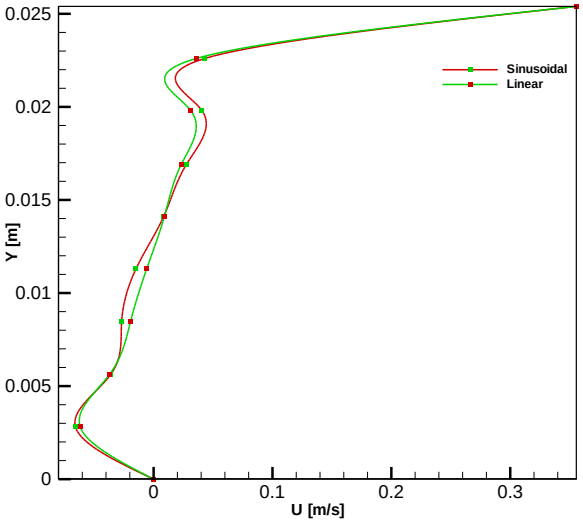

Figure 63-U velocity distribution on the vertical centerline at t=2.4 sec at Re=10 000 for Sinusoidal and linear lid time delays.

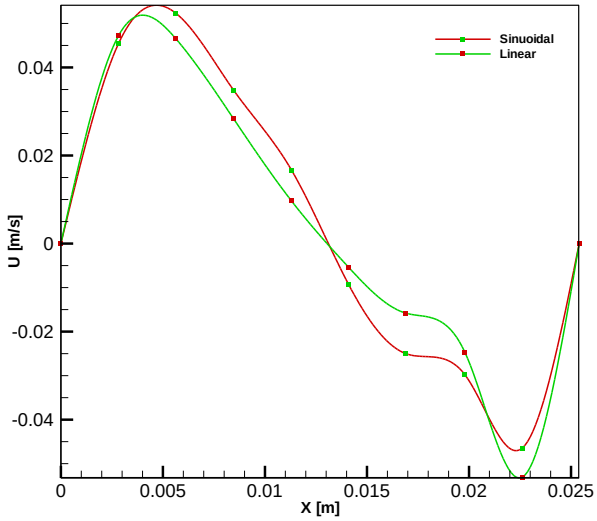

Figure 64-V velocity distribution on the vertical centerline at t=2.4 sec at Re=10 000 for Sinusoidal and linear lid time delays.

Table 21 – Comparing Maximum and Minimum U and V velocities on the vertical and horizontal Centerline Respectively for Linear and Sinusoidal Lid Time Delay of 1.0 sec

Time		**Linear**	**Sinusoidal**
t=0.8	U_{min} [m/s]	-0.026	-0.0159
	U_{max} [m/s]	0.3205	0.2810
	V_{min} [m/s]	-0.0101	-0.0122
	V_{max} [m/s]	0.0075	0.0061
t=1.6	U_{min} [m/s]	-0.0325	-0.0452
	U_{max} [m/s]	0.3560	0.3559
	V_{min} [m/s]	0.0230	0.0335
	V_{max} [m/s]	-0.0510	-0.0452
t=2.4	U_{min} [m/s]	-0.0661	-0.0623
	U_{max} [m/s]	0.3560	0.3530
	V_{min} [m/s]	0.0518	0.0535
	V_{max} [m/s]	-0.053	-0.0452
t=3.6	U_{min} [m/s]	-0.0745	-0.0785
	U_{max} [m/s]	0.3550	0.3235
	V_{min} [m/s]	-0.066	-0.0640
	V_{max} [m/s]	0.0650	0.0730

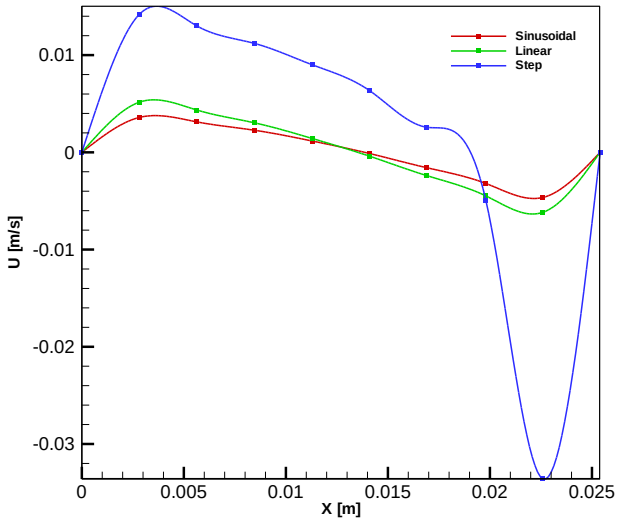

Figure 65- Difference in V velocity ditributions on the horizontal centerline at time, t = 0.8 sec for three different lid accelerations; sinusoidal, linear, step at Re=10,000.

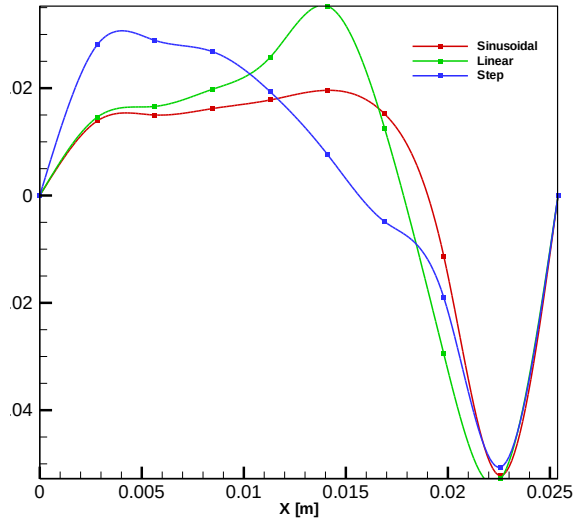

Figure 66- Difference in V velocity ditributions on the horizontal centerline at time, t = 1.6 sec for three different lid accelerations; sinusoidal, linear, step at Re=10,000.

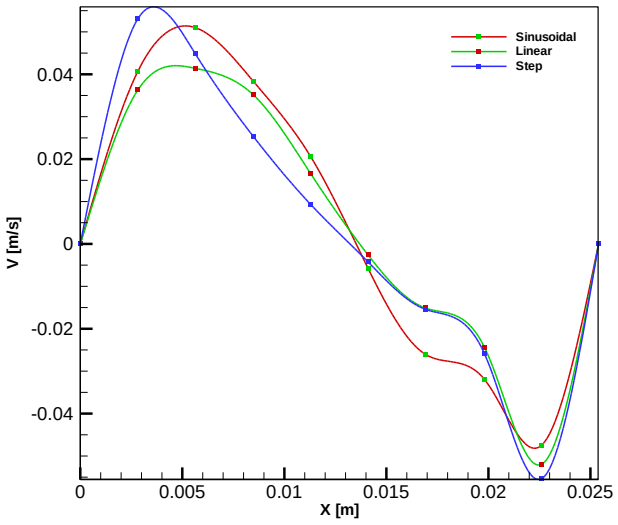

Figure 67- Difference in V velocity ditributions on the horizontal centerline at time, t = 2.4 sec for three different lid accelerations; sinusoidal, linear, step at Re =10,000

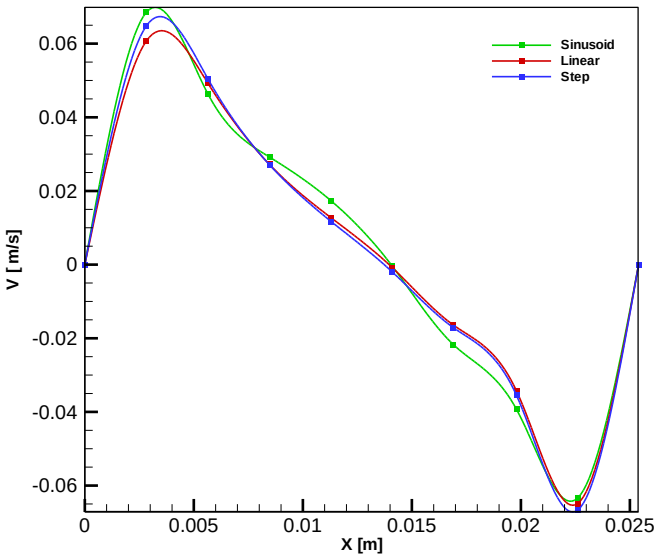

Figure 68- Difference in V velocity ditributions on the horizontal centerline at time, t = 3.6 sec for three different lid accelerations; sinusoidal, linear, step at Re =10,000

Table 22 – Comparing Maximum and Minimum Velocities at different time steps for step linear and sinusoidal delay

Time		**Step**	**Linear**	**Sinusoidal**
t=0.8 sec	V_{max} [m/s]	0.0150	0.0051	0.0038
	V_{min} [m/s]	-0.0335	-0.0060	-0.0045
t=1.6 sec	V_{max} [m/s]	0.0301	0.0355	0.0195
	V_{min} [m/s]	-0.0515	-0.0520	-0.0530
t=2.4 sec	V_{max} [m/s]	0.0551	0.0400	0.0510
	V_{min} [m/s]	-0.0550	-0.0520	-0.0457
t=3.6 sec	V_{max} [m/s]	0.0635	0.0615	0.0700
	V_{min} [m/s]	-0.0670	-0.0650	-0.0635

8. CONCLUSIONS

Experimental and numerical studies were carried out on the lid driven cavity flow for laminar flow regimes. PIV and LDA were employed to measure the local and global velocities, respectively inside the cavity. For the computational study a commercial CFD solver (Fluent) was used. The global velocities measured through the PIV were calibrated with the local velocities measured by the LDA. The experimental results were than compared with CFD predictions in laminar flow regime. For turbulent flow predictions, the Reynolds Averaged Navier Stokes Equations (RANS) together with the K Epsilon closure model were used. Both laminar and turbulent flow models were verified and validated with CFD and experimental results cited in open literature. The following conclusions can be drawn:

1. The PIV measured horizontal velocity distribution on the vertical center line of the cavity agreed well with LDA measured local velocities near the lid for low Reynolds Number in the laminar flow regime.
2. The PIV measured horizontal velocity distribution significantly overestimated the LDA measured local velocities near the geometric center of the cavity for low Reynolds Numbers in the laminar flow regime.
3. The CFD predicted velocity distribution fared well with PIV measured velocity distribution and LDA measured local velocities near the lid but significantly overestimated close to the geometric center of the cavity for laminar flows.
4. By adjusting the coefficient of eddy viscosity, Cmu, it was found the that K Epsilon turbulence model was making predictions in the transition region that converged with laminar solutions at the lower end of the transition region and standard K Epsilon (with default settings) at the upper end and fully turbulent flows.
5. The lid acceleration influenced the flow with sudden velocity peaks at points during the development from stagnation to steady state. The velocity profiles on the vertical and horizontal

centerline also differed in shape between linear and sinusoidal lid accelerations with later producing much sharper gradients along the vertical and horizontal lengths of the cavity.

6. The path the circulation center followed before it reached steady state is also lid velocity dependent, for low Reynolds numbers, this path seems to be close to a straight line. However, during transition to turbulent state, the path starts to be curved and unsteady. This is apparent for Reynolds number 5000. In this case, the center of circulation is unsteady and away from the center of the cavity.

9. **RECOMMENDATIONS**

The following recommendation were made for the present study:

1. Additional experiments should be performed at higher Reynolds Numbers using the PIV.
2. PIV calibration should be carried out at turbulent Reynolds numbers and readings at more local points should be made using the LDA for better results.

REFERENCES

[1] Shankar, P.N. and Deshpande, M.D., 2000, "Fluid Mechanics in the Driven Cavity," Annual Review in Fluid Mechanics, Vol. 32, pp. 93-136.

[2] Koseff, J.R. and Street, R.L., 1984, "The lid driven cavity Flow: a synthesis of qualitative and quantitative observations," Journal of Fluids Engineering, ASME Transactions, Vol. 106, pp. 390-398.

[3] Koseff, J.R. and Street, R.L., 1984, "On the end wall effects in a lid-driven cavity flow," Journal of Fluids Engineering., ASME Transactions, Vol. 106, 385-389.

[3] Koseff, J.R. and Prasad., 1989, "Reynolds Numbers and End Wall Effects on a Lid Driven Cavity Flow," Physics of Fluids., American Institute of Physics, 208 (1989); doi: 10.1063/1.857491

[4] Migeon, C., 2002, "Details on the start-up development of the Taylor-Gortler-like vortices inside a square-section lid –driven cavity for 1,000≤Re≤3,200," Experiments in Fluids, Vol. 33, pp. 594-602.

[5] Liberzon, A., 2011, "On the effects of dilute polymers on driven cavity turbulent flows," International Journal of Heat and Fluid Flow, doi: 10.1016/j.ijheatfluidflow.2011.08.005.

[6] O'Hern, T.J., Torczynski, J.R., Blanchat, T.K., and Chu, T.Y., 1994, "Shear-driven flow in a square cavity: a comparative study using PIV, LDV, and computational simulations," Symposium on Laser Anemometry: Advances and Applications, Proceedings of ASME FED Summer Meeting, June 1994, Lake Tahoe, NV.

[7] Thierry M. Faure "Velocity field and parametric analysis of a subsonic, medium-Reynolds number cavity flow" Experimental Fluids (2014) 55:1822

[8] Tanja-Siegmann-Hegarfeld, S Albensoeder, H C. Kuhlmann (2013) "Three-dimensional flow in a lid driven cavity with width to height ratio of 1.6" Exp Fluids (2013) 54:1526.

[9] Ghia, U., Ghia, K.N., and Shin, C.T., 1982, "High-Re solutions for incompressible flow using the Navier-Stokes equations.

[10] Erturk, E., Corke, T.C., and Gokcol, C., 2005, "Numerical Solutions of 2-D steady incompressible driven cavity flow at high Reynolds numbers," International Journal of Numerical Methods in Fluids, Vol. 48, pp 747-774

[11] E Barragy and G.F.Carey., 1996 "Stream function-vorticity driven cavity solution using p finite elements" Comp & Fluids Vol 26, No.5, pp, 453-468, 1997.

[12] Sahin, M. and Owens, R.G., 2003, "A novel fully implicit finite volume method applied to the lid-driven cavity problem-Part I: High Reynolds number flow calculations" International Journal for Numerical Methods in Fluids, Vol. 42, pp 57-77.

[13] E. Leriche and S. Gavrilakis "Direct numerical simulation of the flow in a lid-driven cubical cavity". Physics of Fluids 12, 1363 (2000); doi: 10.1063/1.870387

[14] S. Pradhan and V. Kumaran "Transition and turbulence in a lid-driven cavity flow at high Mach number" rspa.royalsocietypublishing.org Proc R Soc A 0000000

[15] M.D Deshpanday and S. Milton, 1996 "Kolmogrov Scales in a driven cavity flow" Fluid Dynamics Research 22 (1998) 359-381.

[16] Nagapetyan, T Wray & Rajesh K Agarwal. 2016, “Computation of Turbulent Flow in a Lid Driven 2D cavity and a 3D Box using a number of turbulence models” 5th AIAA Aersospace Science Meeting, San Diego, California, USA

[17] M. Nallasamy, 1986, “Turbulence Models and their applications to the prediction of internal flows, A review. Computers and Fluids” Vol 15 No.2 pp.151-194

[18] Hussain, A., 2016, A Numerical Study of Compressible Lid driven Cavity Flow with a Moving Boundary. MSc Thesis, Dept. of Mech. Engr., University of New Orleans, New Orleans, LA

[19] Akyuzlu, K.M. and Chidurala, M., 2010, “A Numerical Study of Unsteady Natural Convection in a Rectangular Enclosure – Transition from Laminar to Turbulent Flow,” Proceedings of the IMECE2010, Paper No. 37892, Vancouver, B.C., Canada.

[20] Akyuzlu, K.M. and Farkas, J., 2012, “A Study of Formation of Circulation Patterns in Laminar, Unsteady Lid driven Cavity Flows Using PIV Techniques,” Proceedings of the ASME 2012 International Mechanical Engineering Congress and Exposition, Paper No. 86890, Houston, Texas.

[21] Farkas, J., 2011. An Experimental Study of Formation of Circulation Patterns in Laminar, Unsteady Driven Cavity Flows Using PIV Techniques. MSc Thesis, Department of Mechanical Engineering, University of New Orleans, New Orleans, Louisiana.

[22] Akyuzlu, KM. 2017., A Numerical and Experimental Study of Laminar Unsteady Lid-Driven Cavity Flows. proceedings of the ASME 2017 International Mechanical Engineering Congress And Exposition, paper no. 70145, Tampa, Florida

[23] R J Adrian, 2005., “Twenty Years Of Particle Image Velocimetry”. Experiments In Fluids 39:159-169

[24] T Hadad, R Gurka., 2013. “Effects Of Particle Size, Concentration And Surface Coating On Turbulent Flows Properties Obtained Using PIV/PTV,” Experimental And Thermal Fluid Sciences 45 (2013) 203-212.

[25] Tsorng, S.J, Capart, H, Lo, D.C, Lai, J.S, Young, D.L,.2007 “Behavior of macroscopic rigid spheres in lid driven cavity flow”, International Journal of Multiphase Flow, 34(2008)76-101.

[26] Wang, C.P, Sadeghi, F, Werley, S.T, Chuang, H.S, 2009, “Investigation of Fluid Flow out of a microcavity using μ PIV” Tribology Transactions 52:6,817-832, DOI: 10.1080/10402000903125352

[27] Su, W-T and Li,Xiao-Bin. 2013, “Ccomparisons Of Les And Rans Computations With PIV Experiments On A Cylindrical Cavity Flow” Advances In Mechanical Engineering Volume 2013 Article Id: 592940.

[28] A. S Benjamin & V. E Denny, 1979, “On the Convergence of Numerical Solutions for 2D flows in a Cavity at large Reynolds Number” Journal of Computational Physics Volume 22, Issue 3, Pages 340-358.

[30] S.A Jordan and S.A Ragab, 1994,. “On The Unsteady And Turbulent Characteristics Of The Three-Dimensional Shear-Driven Cavity Flow”, J. Fluids Eng, 116(3): 439-449

[31] S.A Jordan and S.A Ragab, 1996,. "A Large-Eddy Simulation of the Shear-Driven Cavity Flow Using Dynamic Modeling", International journal of Computational Fluid Dynamics, Volume 6

[32] M. Nallasamy & K Krishna Prasad, "On Cavity Flow at High Reynolds Numbers", Journal of Fluid Mechanics, Volume 79, Issue 2 22 February 1977 , pp. 391-414

[33] R Schreiber & H.BKeller, 1983,." Driven cavity flows by efficient numerical techniques", Journal of Computational Physics, Volume 49, Issue 2, February 1983, Pages 310-333

[34] Charles-Henri Bruneau & MazenSaad,.2006 " The 2D lid-driven cavity problem revisited, Computers & Fluids, Volume 35, Issue 3 Pages 326-348.

[35] Yih-FerngPenga Yuo-HsienShiaub and Robert R.Hwang,2013,. "Transition in a 2-D lid-driven cavity flow", Computers & Fludis, Volume 32, Issue 3, March 2003, Pages 337-352

[36] Debabrat Samantaray and Manab Kumar Das, 2018,. " High Reynolds Number Incompressible Turbulent Flow Inside A Lid-Driven Cavity With Multiple Aspect Ratios", Physics Of Fluids 30, 075107

[37] Peng Ding,2017,." Solution of Lid Driven Cavity Problem with an improved simple Algorithm at High Reynolds Number", International Journal of Heat and Mass Transfer, Volume 115, Part B, Pages 942-954

[38] P. J. Schmid , K. E. Meyer and O. Pust, 2009,. "Dynamic Mode Decomposition and Proper Orthogonal Decomposition of Flow In A Lid-Driven Cylindrical Cavity", 8th International Symposium On Particle Image Velocimetry - Piv09

[39] Marc Immer, Jonas Allegrini And Jan Carmeliet, 2016,. "Time-Resolved And Time-Averaged Stereo-PIV Measurements Of A Unit-Ratio Cavity" Experiments In Fluids Volume 57, Article Number: 101

[40] J.-L. Guermond, C. Migeon,G. Pineau, and L. Quartapelle,. 2002, "Start-Up Flows In A Three-Dimensional Rectangular Driven Cavity Of Aspect Ratio 1:1:2 At Re = 1000", Journal Of Fluid Mechanics 450:169-199

[41] R. Verstappen, J. G. Wissink and A. E. P. Veldman 1993,. "Direct numerical simulation of driven cavity flows", Applied Scientific Research, Advances in Turbulence IV volume 51, pages377–381

[43] T. Hadad and R. Gurka, 2013,." Effects of particle size, concentration and surface coating on turbulent flow properties obtained using PIV/PTV", Experimental Thermal and Fluid Science Volume 45, February 2013, Pages 203-212

[45] C. Ozalpb, A. Pinarbasia and B.Sahina, 2010,."Experimental measurement of flow past cavities of different shapes", Experimental Thermal and Fluid Science Volume 34, Issue 5 Pages 505-515

[46] A. B. Cortes and J. D. Miller, 1994,. Numerical Experiments With the Lid Driven Cavity Flow problem, Computers & Fluids, Volume 23, Issue 8 Pages 1005-1027

[47] A. Huser and S. Biringen, 1992,. Calculation Of 2d Shear Driven Cavity Flow At High Reynolds Number, Numerical Methods In Fluids, Volume14, Issue9

[48] M.D. Deshpande and S. George Milton, 1998,. “Kolmogrov Scale in a driven Cavity Flow”, Fluid Dynamics Research Volume 22, Issue 6, 1 June 1998, Pages 359-381

Appendix I

Vector Form of Governing Differential Equations

Continuity Equation:

$$\frac{D\rho}{Dt} + \rho(\nabla . \vec{u}) = 0$$

Momentum Equation:

$$\frac{\rho D\vec{u}}{Dt} = \rho\vec{g} - \nabla P + \nabla . \tau'_{ij}$$

Where Shear Stress term is given by:

$$\tau'_{ij} = \mu\left(\frac{du_i}{dx_j} + \frac{du_j}{dx_i}\right) - \frac{2}{3}\mu\left(\frac{du_k}{dx_k}\right)\delta_{ij}$$

The Kronecker delta is given by:

$$\delta_{ij} = \begin{cases} 1 \; i = j \\ 0 \; i \neq j \end{cases}$$

Appendix II

Run Matrix for the Numerical Simulation

Problem Setup	Options				
General	Mesh	Scale			
		Check			
		Report Quality			
		Display			
	Solver	Type	Pressure-Based		
			Density-Based		
		Velocity Formulation	Absolute		
			Relative		
		Time	Steady		
			Transient		
	Gravity: uncheck				
Models	Multiphase: Off				
	Energy: OFF				
	Viscous: Standard, k-e, Standard Wall				
	Radiation: Off				
	Heat Exchanger: Off				
	Species: Off				
	Discrete Phase: Off				
	Solidification & Melting: Off				
	Acoustics: Off				
Materials	Fluid	Water			
	Solid: Aluminum (NA)				
Cell Zone Conditions	Working Fluid	Material name	Water, Liquid		
Boundary Conditions	Zone	Lid Type: Wall	Wall Motion	Moving Wall	
			Motion	Absolute	
				Translation	
			Speed (m/s)	0.3956	
			Direction	x = 1	
			Shear Condition	No Slip	
			Wall Roughness	Roughness Height (m) = 0	
				Roughness Constant = 0.5	
		Interior-Surface-Body			
		Walls Type: Wall	Wall Motion	Stationary wall	
			Shear Condition	No Slip	
			Wall Roughness	Roughness Height (m) = 0	
				Roughness Constant = 0.5	

Dynamic Mesh	Dynamic Mesh: check (Layering)		
Reference Values	Compute Form	Inner Fluid	
		Inlet	
		Interior-Inner Fluid	
		Outlet	
		Surface	
	Reference Values	All calculated with the boundary conditions provided.	
Solution			
Solution Methods	Pressure- Velocity Coupling	Scheme	SIMPLE
			SIMPLEC
			PISO
			Coupled
	Spatial Discretization	Gradient	Green-Gauss Cell Based
			Green-Gauss Node Based
			Least Squares Cell Based
		Pressure	Standard
			PRESTO!
			Linear
			Second Order
			Body Force Weighted
		Density	First Order Upwind
			Second Order Upwind
			QUICK
			Third-Order MUSCL
		Momentum	First Order Upwind
			Second Order Upwind
			Power Law
			QUICK
			Third-Order MUSCL
		Turbulent Kinetic Energy	First Order Upwind
			Second Order Upwind
			Power Law
			QUICK
			Third-Order MUSCL
		Turbulent Dissipation Rate	First Order Upwind
			Second Order Upwind
			Power Law
			QUICK
			Third-Order MUSCL

Solution Control	Courant Number: 200	
	Explicit Relaxation Factors	Momentum: 0.75
		Pressure: 0.75
	Under Relaxation Factors	Density:1
		Body Forces: 1
		Turbulent Kinetic Energy: 1
		Turbulent Dissipation Rate: 1
		Turbulent Viscosity: 1
		Energy: 1
Monitors	Residuals, Statistics and Force Monitors	Residuals- Prints, Plots: 1e-15
Solution Initializations	Compute form	All-Zones
		Inlet
		Outlet
		Surface
	Initial Values	Gauge Pressure (Pascal): 0 Other values for initial velocity, temperature are calculated according to the given boundary conditions.
Calculation Activities	Auto save every iteration = 10	
Run Calculations	Check case Number if Iterations:2000 Calculate	

Appendix III

Run Matrix for the PIV Post Processing

Run Name		Study
A1-4		Spot Mask Engine
Common Post Processing Parameters Grid Engine: Nyquist Grid Spot Mast Engine: Correlation Engine: Hart Correlator Peak Engine: Gaussian Peak Starting Spot Size Dimension: 32x32 Overlay: 50%	1.	Deformation Mask
	2.	Gaussian Mask
	3.	No Mask
	4.	Zero Pad Mask
B1-3		Correlation Engine
Common Post Processing Parameters Grid Engine: Nyquist Grid Spot Mast Engine: No Mask Correlation Engine: Peak Engine: Gaussian Peak Starting Spot Size Dimension: 32x32 Overlay 50%	1.	Hart Correlator
	2.	Direct Correlator
	3.	FFT Correlator
C1-3		Peak Engine
Common Post Processing Parameters Grid Engine: Nyquist Grid Spot Mast Engine: No Mask Correlation Engine: Hart Correlator Peak Engine: Starting Spot Size Dimension: 32x32 Overlay: 50%	1.	Bilinear Peak
	2.	Brownian Temperature Peak
	3.	Gaussian Peak
D1-3		Starting Spot Size Dimension
Common Post Processing Parameters Grid Engine: Nyquist Grid Spot Mast Engine: No Mask Correlation Engine: Hart Correlator Peak Engine: Gaussian Peak Starting Spot Size Dimension: Overlay: 50%	1.	16 x 16
	2.	32 x 32
	3.	64 x 64
E1-3		Overlay
Common Post Processing Parameters Grid Engine: Nyquist Grid	1.	25%

Spot Mast Engine: No Mask Correlation Engine: Hart Correlator Peak Engine: Gaussian Peak Starting Spot Size Dimension: 32x32 Overlay:	2.	50%
	3.	75%

Appendix IV

Engineering Drawings & CAD Modeling

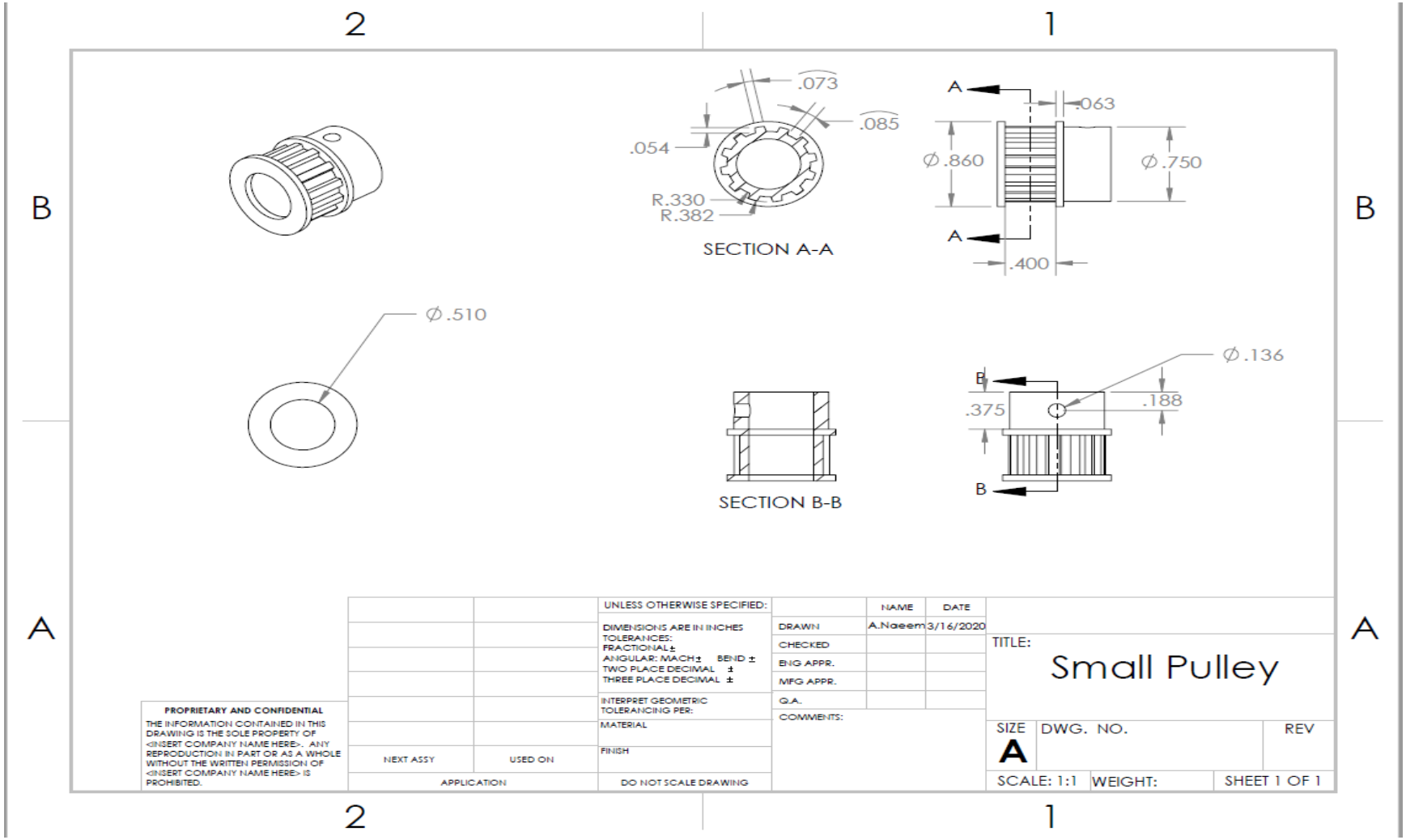

Figure 69- Engineering Drawing for the Small Pulley (Designed for 3D Printing)

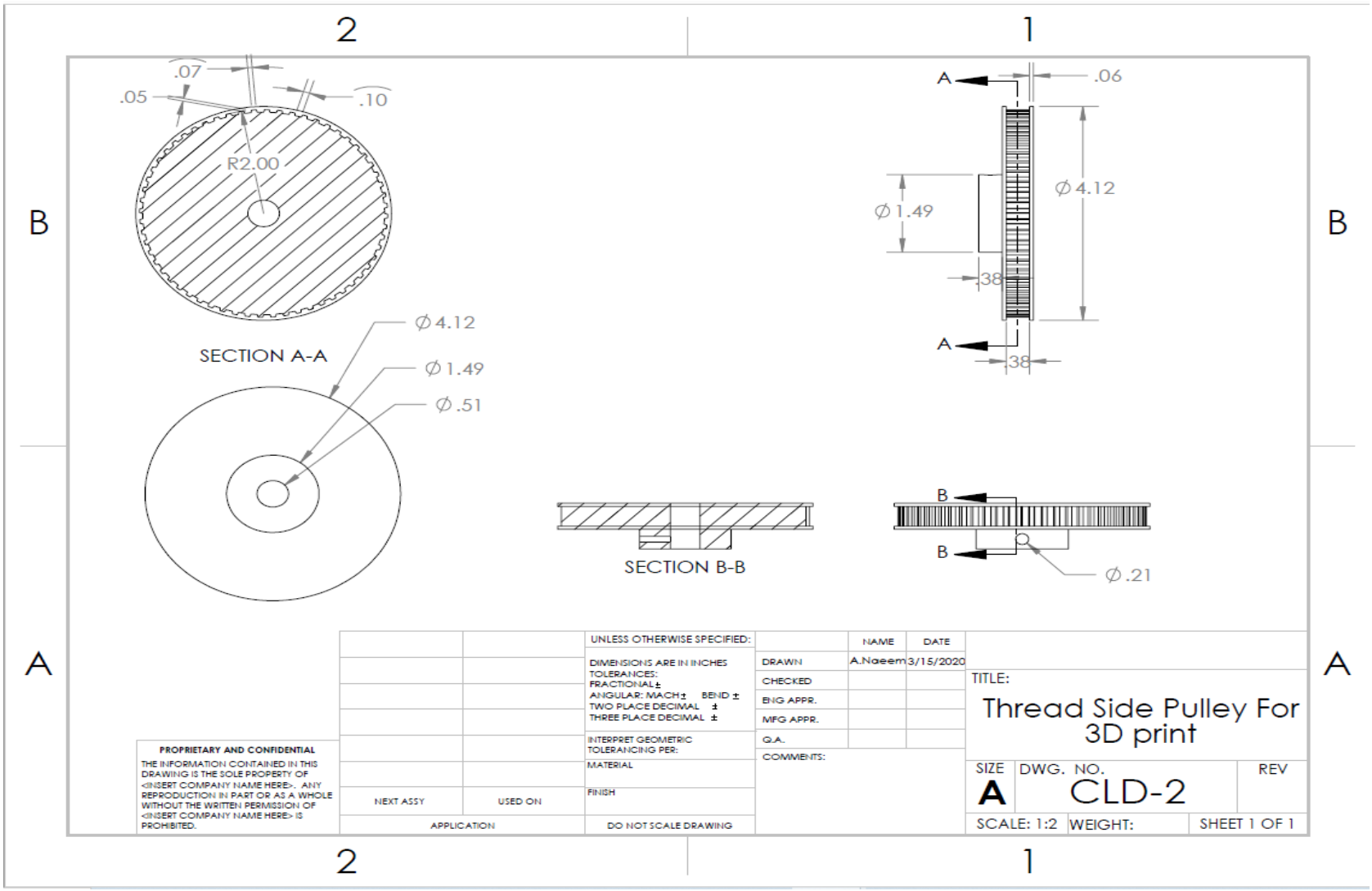

Figure 70- Engineering Drawing for the Large Pulley (Designed for 3D Printing)

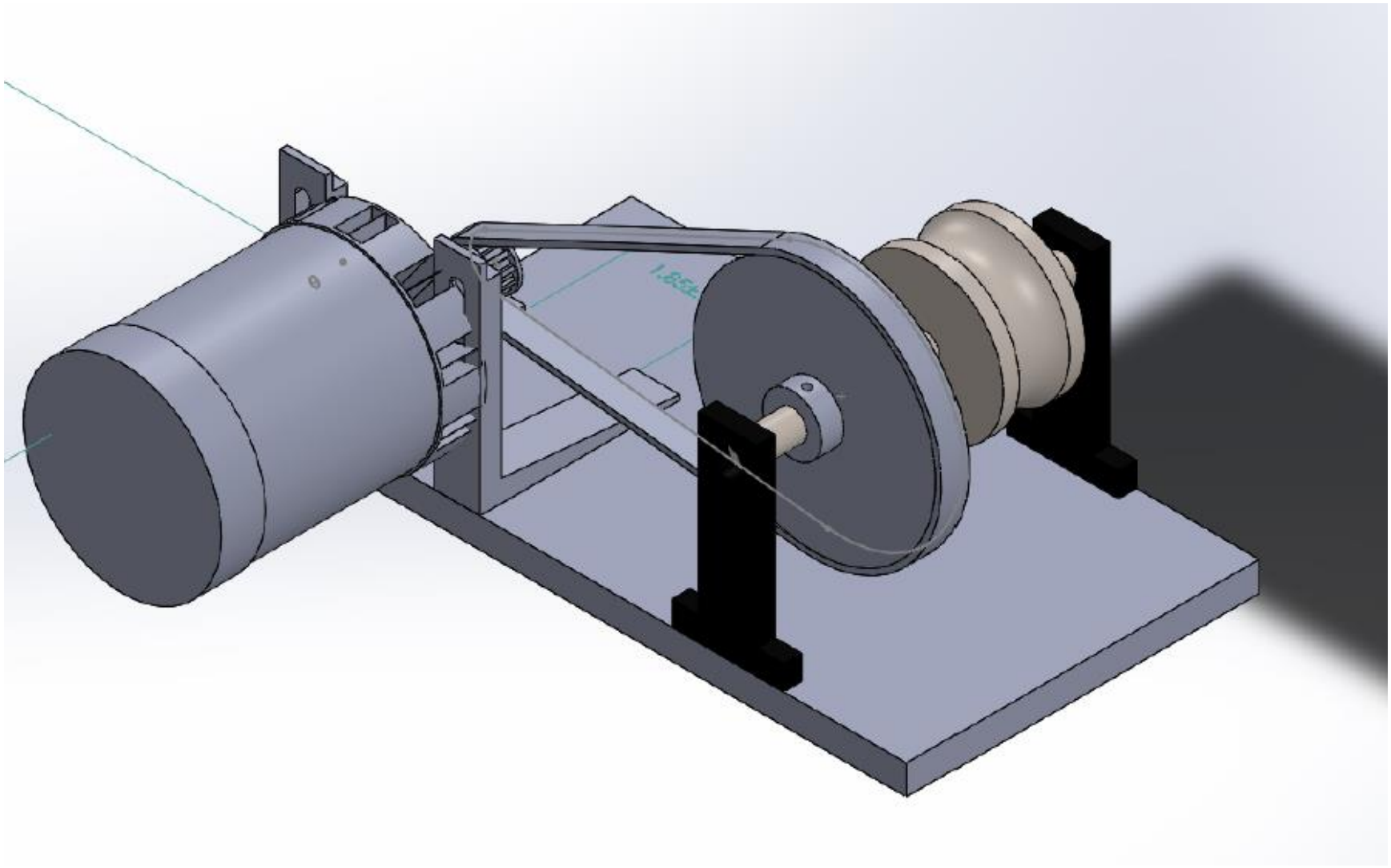

Figure 71- 3D Model of the Lid Driven Cavity Flow Driver Mechanism

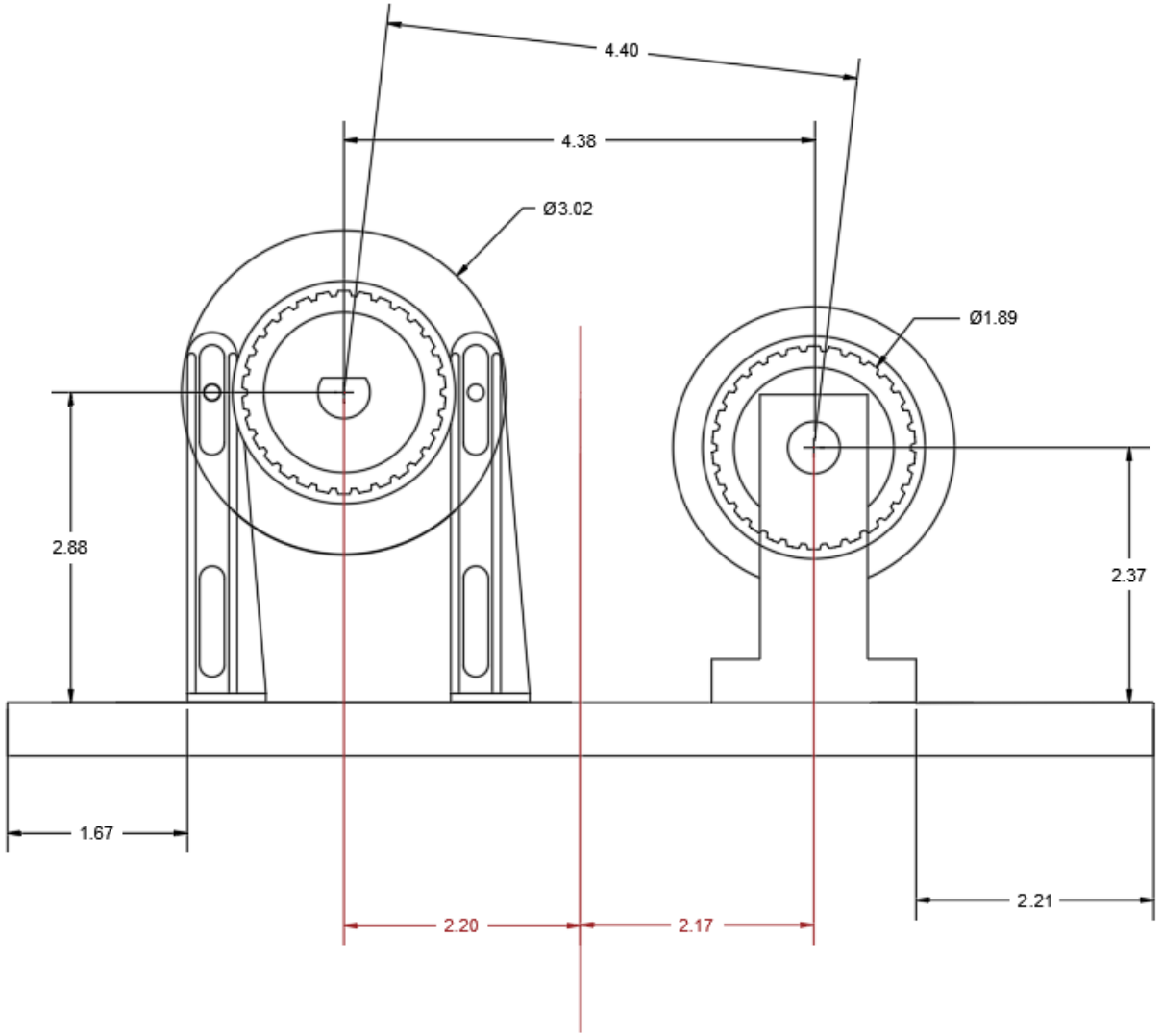

Figure 72 – Driver Mechanism for the Lid Driven Cavity Flow, Front View

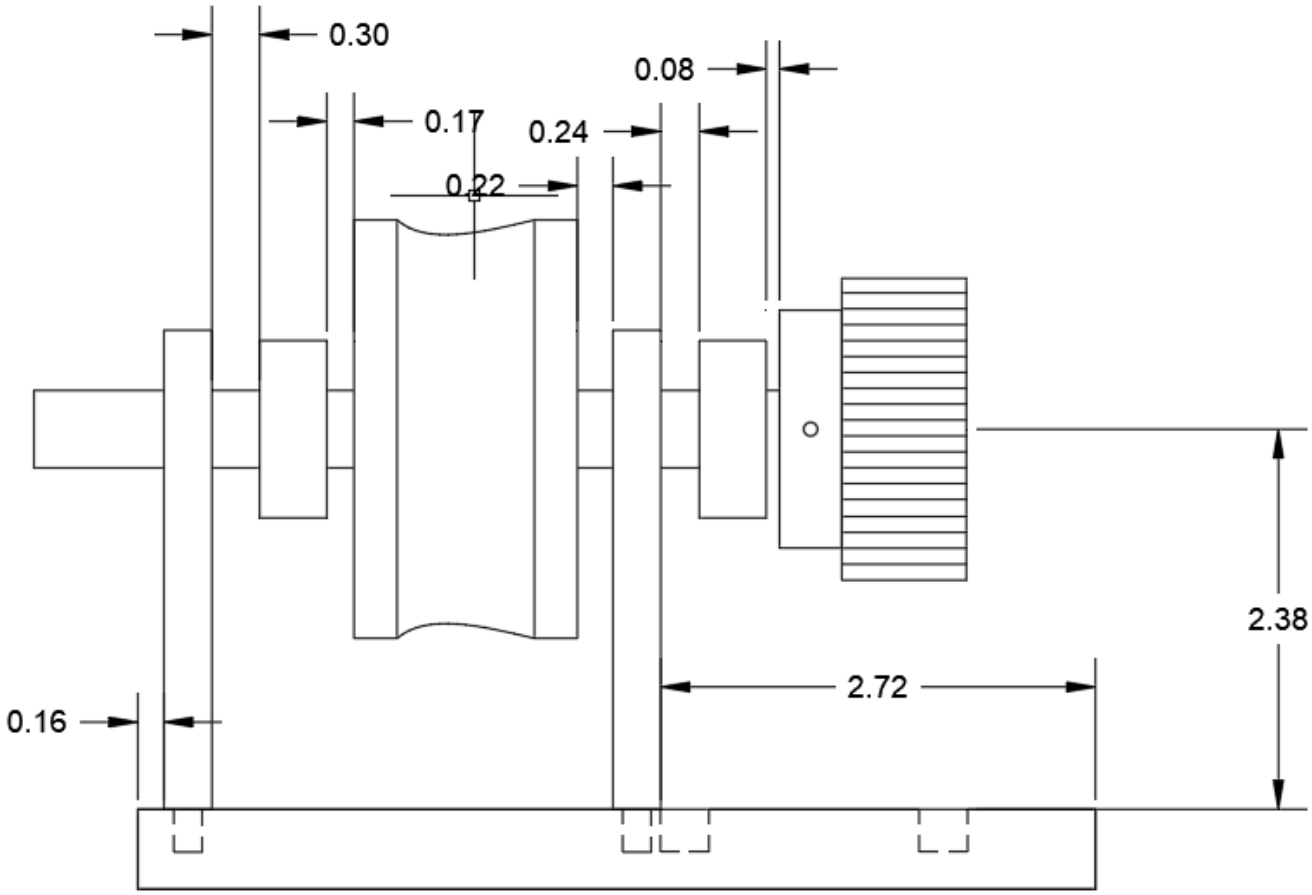

Figure 73 – Driver Mechanism for the Lid Driven Cavity Flow, Side View

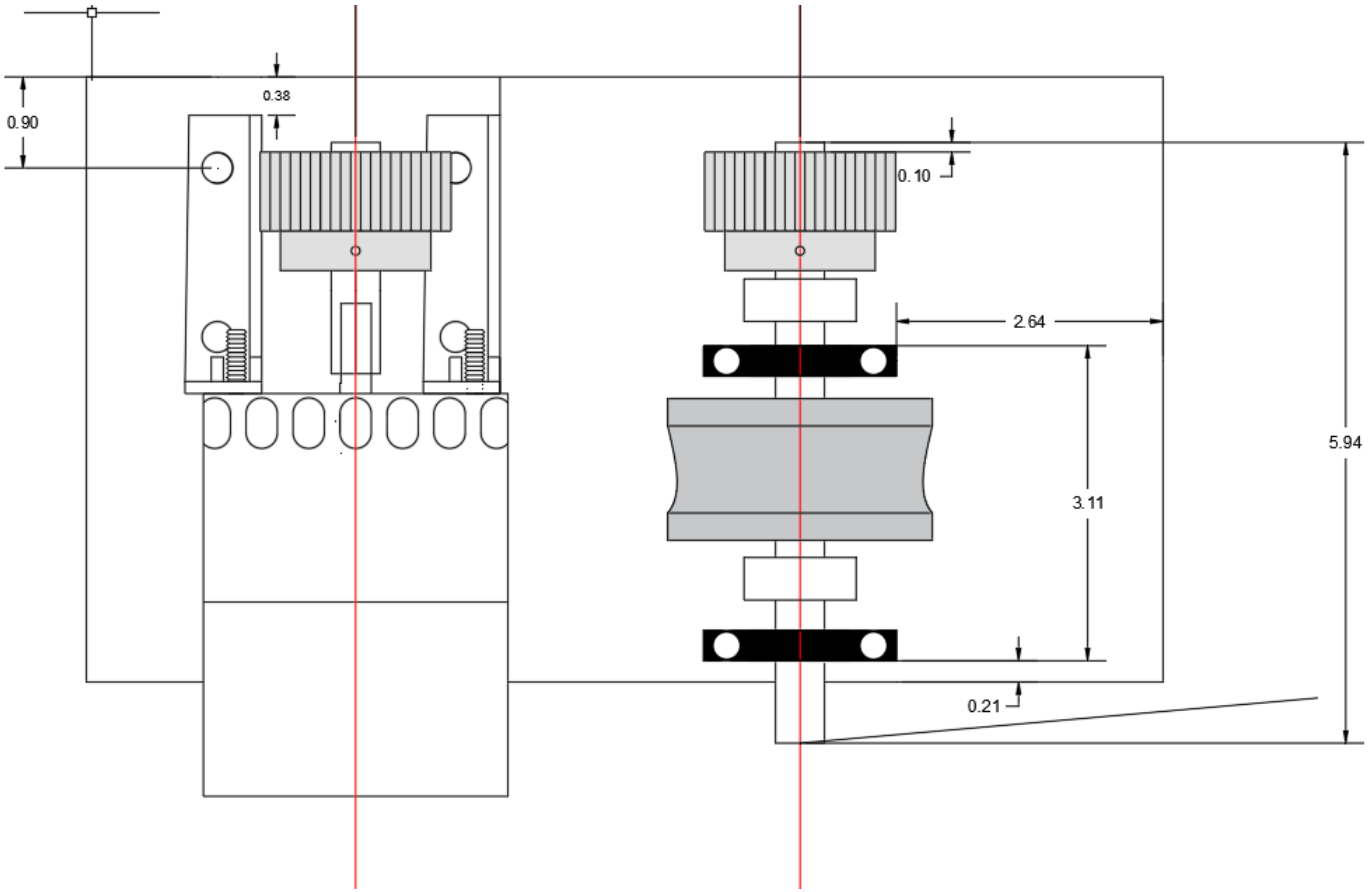

Figure 74 – Driver Mechanism for the Lid Driven Cavity Flow, Top View

Appendix V

User defined Function for Lid Velocity Profile

```
#include "udf.h"

DEFINE_PROFILE(unsteady_velocity, thread, position)
{
  face_t f;

  double period =1;
  double Umax = 0.1;

  begin_f_loop(f, thread)
    {
      real t = RP_Get_Real("flow-time");
            if(t<period)
      F_PROFILE(f,thread, position) = Umax*(0.1+0.1*sin((3.142/period)*t-1.571));
      else if(t>period)
            F_PROFILE(f,thread,position)=Umax;
    }
  end_f_loop(f, thread)
}s
```

Appendix VI

Equipment List

PIV Equipment List:

1. Laser, New Wave Solo 200XT w/532 & 266nm
2. Laser Pulse Synchronizer
3. Power view Plus 4MP Camera Systems
4. Lens 60mm F/2.8 AF Micro – Nikor
5. 532 nm Bandpass Filter
6. Module3G-2DPIV INSIGHT3G Module 2D PIV
7. Computer PIV Dual Xeon 3 GHz 4GB 2x250GB
8. Dichroic Mirror, sep 532 from 350-500nm
9. Frame Grabber PC- CAMLINK PCI
10. Cable Asy Powerview 2M Trigger.

LDA Equipment List:

1. Laser System (Argon Ion Laser 2017) With Remote Control Unit
2. Mounting Base Rail and Mounts
3. Fiber light
4. Transceiver
5. Photo detector module – PDM 1000
6. Multibit digital intensifier- FSA4000
7. Single Probe LDV Mount Kit
8. Rail Hardware Kit
9. Computer
10. Traverse Mechanism with Hand Control Unit

VITA

The author was born in the city of Lahore, Pakistan and passed his early schooling and college from Lahore. He obtained his bachelor's degree in Industrial Engineering in 2013 from University of Engineering & Technology, Lahore. He Joined University of New Orleans in Spring 2018 for his master's in mechanical engineering and is currently pursuing a Phd in Engineering Sciences.